POLITECNICO DI TORINO

Master of Science
in Energy and Nuclear Engineering

Master Thesis

# Design, manufacture, test and simulations of W7-X divertor tiles realized in Additive Manufacturing


*Supervisors*:
Prof. Laura Savoldi
Dr. Joris Fellinger
Ing. Alessio Quamori Tanzi

*Candidate*:
Andrea Picchio


Academic Year 2025/2026

*To my grandparents*

**Ringraziamenti**

Desidero esprimere la mia più sincera gratitudine alla Professoressa Laura Savoldi, all'Ingegnere Alessio Quamori Tanzi e al Dr. Joris Fellinger per la guida attenta, la disponibilità e i preziosi consigli che mi hanno accompagnato nel corso di questa tesi.

Un ringraziamento speciale va alla mia famiglia, che mi ha sostenuto e incoraggiato nei momenti felici e in quelli più difficili durante i miei anni di studio, insegnandomi la tenacia necessaria per portare a termine questo percorso. Con loro ho condiviso gioie e difficoltà, e questo traguardo è anche loro. Il loro affetto e la loro presenza costante hanno reso possibile questo risultato.

Ringrazio inoltre i miei amici per il sostegno costante e l'incoraggiamento che mi hanno dato durante il mio percorso di studi. Questo traguardo non sarebbe stato possibile senza di loro.

# Abstract

In nuclear fusion devices such as the Wendelstein 7-X (W7-X) stellarator, the divertor is a critical component responsible for particle and heat exhaust. It consists of multiple target elements (tiles) that intercept plasma particles and must withstand extremely high thermal loads, up to 20 $MW/m^2$. The divertor geometry is designed to spread the heat flux over a larger surface while maintaining structural integrity under severe operating conditions.

This thesis investigates the thermo-hydraulic performance of simplified version of a divertor tile based on Triply Periodic Minimal Surfaces (TPMS), realized through Additive manufacturing (AM). TPMS geometries offer a promising solution for enhancing convective heat transfer while minimizing pressure losses.

A key challenge associated with Additive Manufacturing (AM) is the presence of geometric inaccuracies and residual surface roughness, which may affect both hydraulic and thermal behavior. To assess these effects, a validation study was conducted based on an experimental campaign performed at Politecnico di Milano. The experimental data were compared with Computational Fluid Dynamics (CFD) simulations, showing good agreement. The numerical results did not require the inclusion of a roughness model, indicating high manufacturing quality with negligible residual roughness.

Following validation, simulations were carried out under representative operating conditions. The results demonstrate that the Gyroid TPMS geometry is well suited for high heat flux applications, maintaining solid temperatures below the safety limit of 450°C under both nominal conditions (10 $MW/m^2$) and extreme loads up to 20 $MW/m^2$.

Due to the geometric complexity of TPMS structures and the required operating mass flow rates, directly modeling surface roughness would necessitate a high-$y^+$ wall treatment, which in this case is not feasible. Therefore, the effect of roughness was investigated using a set of simplified channel geometries. The turbulence model was first validated against analytical solutions for fully developed flow in a circular pipe, and subsequently applied to more complex configurations. Further experimental validation will be required to confirm these findings.

# Contents

# List of Figures

# List of Tables

# Acronyms

**AM** Additive Manufacturing.

**CAD** Computer-Aided Design.

**CFD** Computational Fluid Dynamics.

**CNC** Computer Numerical Control.

**ECRH** Electron Cyclotron Resonance Heating.

**EDM** Electrical Discharge Machining.

**FDM** Fused Deposition Modeling.

**GCI** Grid Convergence Index.

**HHF** High Heat Flux.

**HT** Heat Treated.

**HTC** Heat Transfer Coefficient.

**IAPWS-IF97** International Association for the Properties of Water and Steam.

**ICRH** Ion Cyclotron Resonance Heating.

**L-PBF** Laser Powder Bed Fusion.

**NBI** Neutral Beam Injection.

**NiTi** Nickel-Titanium alloy.

**PBF** Powder Bed Fusion.

**RANS** Reynolds-Averaged Navier-Stokes.

**SLA** Stereolithography.

**SLM** Selective Laser Melting.

**SLS** Selective Laser Sintering.

**TPMS** Triply Periodic Minimal Surfaces.

**W7-X** Wendelstein 7-X.

**WEDM** Wire Electrical Discharge Machining.

# Glossary

$D_h$ Hydraulic diameter.

$R^+$ Roughness parameter.

$R^+_{\mathbf{rough}}$ Rough roughness limit.

$R^+_{\mathbf{smooth}}$ Smooth roughness limit.

$\alpha$ Deformation parameter.

$\beta$ Deformation parameter.

$\kappa$ von Kármán constant.

$\lambda$ Thermal conductivity.

$\mu$ Dynamic viscosity.

$\mu_t$ Turbulent viscosity.

$\mu_{t,t}$ Turbulent viscosity (outer region).

$\mu_{t,v}$ Turbulent viscosity (inner region).

$\phi$ Interpolation parameter.

$\rho$ Density.

$\varepsilon$ Turbulent dissipation rate.

$\varphi$ Porosity.

$c_p$ Specific heat.

$f$ Friction factor.

$h$ Specific enthalpy.

$k$ Turbulent kinetic energy.

$r$ Sand-grain roughness height.

$u^+$ Dimensionless velocity.

$u_*$ Velocity scale.

$y^+$ Dimensionless distance from wall.

$\Delta p$ Pressure drop.

**Nu** Nusselt number.

**Re** Reynolds number.

# 1 Introduction

## 1.1 W7-X fusion reactor

The Wendelstein 7-X (W7-X) was conceived with the aim of assessing the feasibility of optimized stellarators as a solution for future fusion reactors [1], [2]. This device adopts quasi-symmetric magnetic configurations, designed through advanced optimization techniques in order to reduce losses compared to a tokamak [1], [2].

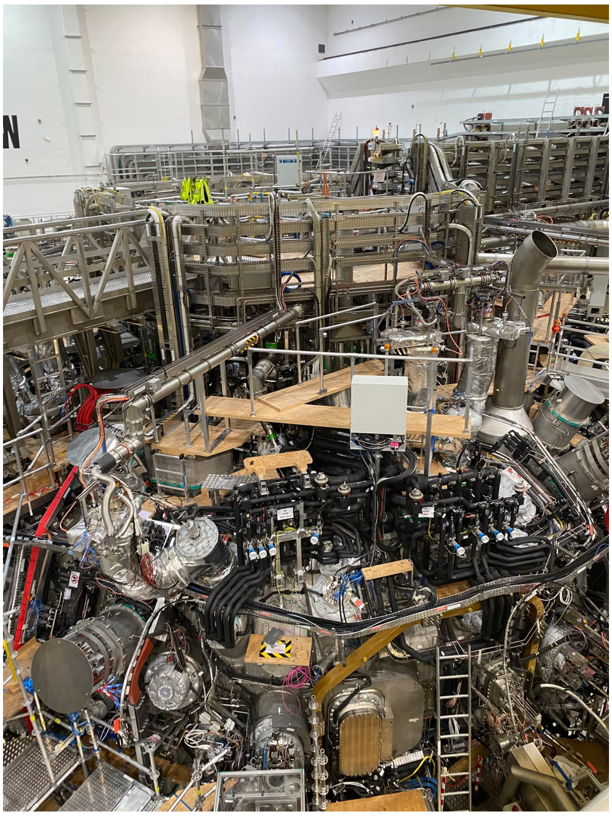

Figure 1: W7-X fusion reactor

Plasma confinement is achieved by means of a system of 70 superconducting coils made of NbTi alloy, maintained at approximately 4.5 K through liquid helium cooling [1]. The coils are arranged in five identical modules to preserve the typical stellarator symmetry and can be divided into: 50 non-planar coils, characterized by a highly complex three-dimensional geometry, responsible for generating the main magnetic field and for shaping the helical plasma configuration; 20 planar coils, used to adjust the toroidal component of the magnetic field and to control the rotational transform.

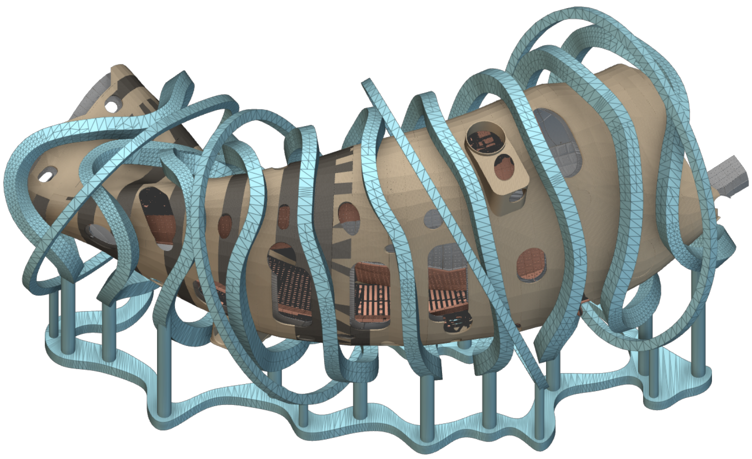

Figure 2: W7-X plasma vessel and coils [3]

The possibility of independently varying the currents in the different coils provides the device with a high degree of operational flexibility, allowing the exploration of different magnetic configurations (such as the "standard" or "high-mirror" configurations) in order to optimize key parameters, including the bootstrap current and fast ion confinement. Plasma heating is mainly provided by Electron Cyclotron Resonance Heating (ECRH), supported by Neutral Beam Injection (NBI) and Ion Cyclotron Resonance Heating (ICRH) [1].

Regarding particle and heat exhaust, W7-X employs the island divertor concept, which differs from the tokamak approach where the separatrix is axisymmetric. In stellarators, the three-dimensional magnetic topology naturally generates magnetic island chains at the plasma edge, associated with rational values of the rotational transform [4], [5]. These structures, characterized by X-points and O-points, develop along helical trajectories around the plasma column.

The divertor architecture is organized hierarchically into divertor units, each composed of several modules, which in turn are assembled from individual tiles, as schematically shown in Figure 4. This modular arrangement enables a distributed management of the heat exhaust while keeping the mechanical and hydraulic design localized within each unit [6], [7].

Recently, alternative cooling concepts based on sub-millimeter microchannels manufactured through additive manufacturing have emerged as credible solutions from both thermal-hydraulic and thermo-mechanical perspectives [8]. Nevertheless, TPMS-based cooling structures appear to be a more promising solution, as they can provide a favorable compromise between heat transfer enhancement, hydraulic performance, and manufacturability.

The tile has a toroidal width of 10 cm and a poloidal extension of 30 cm, which is consistent with the geometry adopted in Reference [6]. It features a layered structure composed of a tungsten armor, a soft copper interlayer, and a CuCrZr substrate hosting the cooling architecture. The coolant, subcooled water at 30 °C, enters and leaves through dedicated ducts on the back side of the tile, as schematically indicated in Reference [6]. Compared with the standard 10 cm $\times$ 10 cm tile layout, the longer poloidal extent reduces the number of hydraulic interconnections required on the rear side of the divertor, thereby simplifying the plumbing and limiting the associated pressure losses.

The cooling concept is designed to remove a steady-state heat flux of 10 MW/m$^2$ over a maximum poloidal heated length of 10 cm [6]. Heat must be extracted while keeping the coolant as close as possible to a single-phase regime, so as to avoid approaching the critical heat flux region and the onset of film boiling. For this reason, the cooling structure is designed so that the temperature at the solid-fluid interface remains below the saturation temperature, evaluated conservatively at the outlet pressure [6]. In addition, the use of the existing water-supply infrastructure is preferred, in order to avoid changes outside the machine and the related increase in cost. In this framework, the available supply lines impose a flow-rate limit and a maximum admissible pressure drop that strongly constrain the design [6].

The present work therefore adopts a simplified design approach, aimed at facilitating manufacturing and experimental validation while retaining the essential thermal-hydraulic features of the proposed cooling concept.

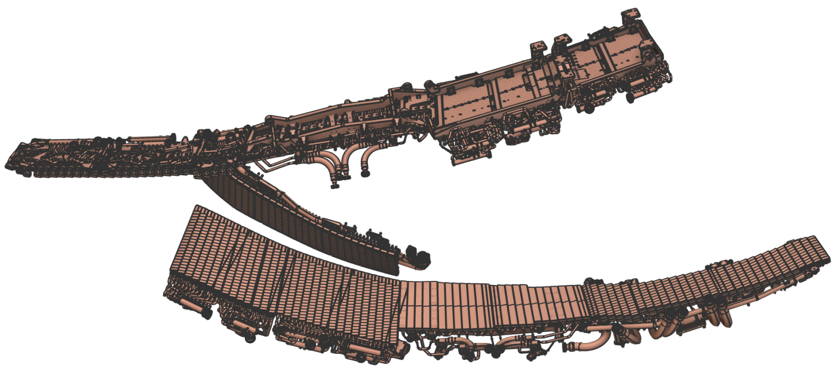

Figure 3: W7-X divertor [3]

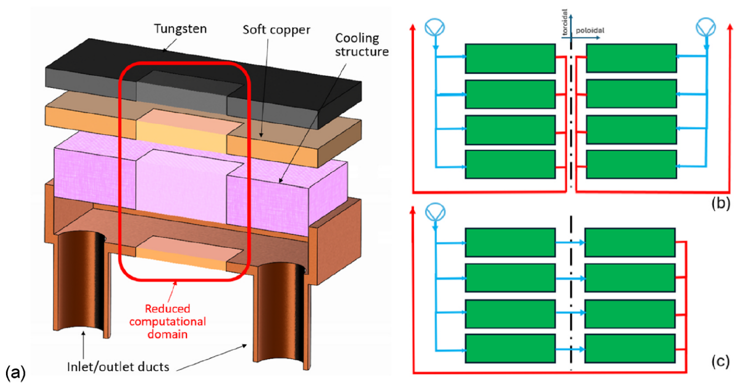


Figure 4: W7-X divertor tile layout [6]

## 1.2 TPMS

Triply Periodic Minimal Surfaces (TPMS) are continuous mathematical surfaces characterized by zero mean curvature at every point and by the absence of self-intersections [6], [9]. From a geometric standpoint, they are periodic along three orthogonal spatial directions, meaning that they repeat infinitely in three-dimensional space without intersecting or overlapping, thereby partitioning the domain into identical and interconnected units [9]. The term "minimal" derives from their mathematical property of minimizing surface area under given symmetry and volume constraints [10], [11]. These complex architectures are commonly described through level-set approximation equations, which combine trigonometric functions, such as sine and cosine, in the three spatial dimensions [6], [12], [13]. Since these are periodic structures, a unit cell is defined to describe the TPMS geometry.

Several TPMS types exist; among the most widely studied in engineering are the Gyroid (G), the Diamond (D), and the Primitive, which are the most general and commonly used, while other configurations include the Neovius and the Fischer-Koch S.

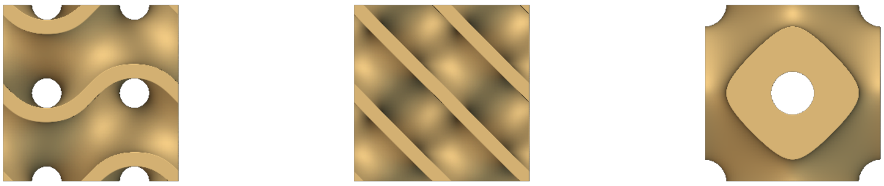

Figure 5: Gyroid, diamond and primitive configuration [14]

Their equations are reported below [7]:

$$\text{Gyroid:} \quad \sin(x)\cos(y) + \sin(y)\cos(z) + \sin(z)\cos(x) = C \tag{1}$$

$$\begin{aligned}\text{Diamond:} \quad & \sin(x)\sin(y)\sin(z) + \sin(x)\cos(y)\cos(z) \\ & + \cos(x)\sin(y)\cos(z) + \cos(x)\cos(y)\sin(z) = C\end{aligned} \tag{2}$$

$$\text{Primitive:} \quad \cos(x) + \cos(y) + \cos(z) = C \tag{3}$$

$$\text{Neovius:} \quad 3[\cos(x) + \cos(y) + \cos(z)] + 4\cos(x)\cos(y)\cos(z) = C \tag{4}$$

$$\begin{aligned}\text{Fischer-Koch S:} \quad & \cos(4\pi x)\sin(2\pi y)\cos(2\pi z) \\ & + \cos(2\pi x)\cos(4\pi y)\sin(2\pi z) \\ & + \sin(2\pi x)\cos(2\pi y)\cos(4\pi z) = C\end{aligned} \tag{5}$$

To further enhance heat transfer and control fluid dynamics, these equations can be modified to create hybrid and deformed topologies. Hybrid structures arise from the connection of two standard surfaces, combined mathematically through an interpolation function using a parameter $\phi$ that varies between 0 and 1 [15], [16]. The resulting expression is:

$$F_{Hybrid} = \phi F_{surface\,1} + (1 - \phi)F_{surface\,2} \tag{6}$$

In deformed geometries, instead, the classical TPMS equation is altered by introducing a control term that geometrically modifies the curvature while preserving the continuous nature of the structure.

For each geometry type, it is also possible to choose between two variants: sheet structures and solid structures. In the former case, the ideal surface is extruded with a certain thickness on both sides, creating two intertwined but non-communicating flow channels [10], [6], [17]. In solid structures, one of the two previously described channels is completely filled with solid material, forming a single complex network through which the fluid flows. Sheet structures are particularly advantageous for heat transfer compared with solid ones because they provide an interfacial area that is approximately twice that of solid models. The general form of these functions is $F(x, y, z) = C$, where the constant $C$ represents the level-set parameter that determines and controls the porosity [12], [18]. This leads to:

$$\text{solid networks:} \quad F(x, y, z) - C = 0 \tag{7}$$

$$\text{sheet networks:} \quad [F(x, y, z)]^2 - C^2 = 0 \tag{8}$$

TPMS structures exhibit unique thermophysical, hydraulic, and mechanical properties that make them clearly superior to traditional cellular geometries. One of their most distinctive features is the extremely high surface-to-volume ratio: they can provide an exceptional surface density within a very compact volume, thereby maximizing heat and mass transfer [12], [13], [19], [20]. From a fluid-dynamic perspective, the absence of sharp edges and the presence of smooth curvatures significantly reduce friction losses and prevent the formation of dead zones where the fluid may stagnate [10], [20]. In addition, the tortuous path of the internal channels continuously disrupts the thermal boundary layer and induces helical secondary flows, promoting excellent mixing and significantly increasing convective heat transfer coefficients [21], [22], [17].

Another major advantage is the high controllability of the design: thanks to their mathematical description, it is possible to modify both locally and globally parameters such as unit cell size, wall thickness, and porosity, adapting the structure to specific engineering requirements [23], [12], [9]. From a mechanical perspective, these self-supporting geometries with zero mean curvature distribute stresses more uniformly, avoiding stress concentrations and thus providing higher structural strength and a greater elastic modulus [24].

The complexity of TPMS channels forces the fluid to follow highly tortuous paths. This continuous deviation causes periodic boundary-layer separation and reattachment, leading to impacts against the solid walls. According to the conservation of energy, this continuous loss of kinetic energy in the fluid is compensated by a significant pressure drop. In addition, geometries with less rounded corners and strongly irregular cross-sections promote flow separation and the formation of large recirculation zones, increasing frictional resistance. Pressure losses vary significantly depending on the TPMS type: Primitive structures generally exhibit the lowest pressure losses, followed by Gyroid and Diamond, and finally by more advanced geometries, which lead to more extreme pressure drops. For the same cell dimensions, sheet networks generate higher pressure drops than solid networks. Since the sheet structure divides the space into two separate flows, it halves the effective pore size and doubles the friction area for the fluid [13]. Although they dissipate much more heat, sheet networks require substantial pumping power.

Two design parameters directly influence the hydraulic behavior of TPMS structures. The first is porosity, defined as:

$$\varphi = \frac{V_{fluid}}{V_{tot}} \tag{9}$$

where $V_{fluid}$ and $V_{tot}$ represent the fluid volume and the total available volume, assuming no TPMS structure is present. This quantity therefore ranges from 0 to 1. Porosity is strongly inversely correlated with pressure losses: a reduction in porosity leads to narrower flow passages and, for a fixed flow rate, forces the fluid to accelerate significantly, resulting in a non-linear increase in pressure losses, often proportional to the square of velocity [25]. Similarly, the unit cell size plays a crucial role: reducing it at constant global porosity results in a denser lattice and a marked increase in specific surface area, intensifying the formation of vortices and helical flow structures and thereby causing larger pressure drops [26]. The flow direction relative to the geometry and any lattice offset also have a significant impact.

To mitigate these effects, several strategies have been developed to reduce pressure losses while maintaining good thermal performance. Controlled geometric deformation through parameters such as $\alpha$ and $\beta$ allows, in the case of the Gyroid, pressure-drop reductions on the order of 5–14%, thanks to a guiding effect that limits boundary-layer separation, although excessive deformation becomes counterproductive [22], [27]. Hybrid structures, obtained by combining different TPMS types such as Gyroid and Diamond, tend instead to introduce geometric discontinuities that generate chaotic turbulence and can drastically increase pressure losses, up to values 391% higher than those of simpler configurations [15]. Finally, topology optimization based on fluid-dynamic algorithms makes it possible to modulate material distribution and porosity in space, accommodating flow expansion and reducing pressure losses by as much as 33% compared with uniform TPMS structures [13].

The fabrication of TPMS structures is one of the most complex and fascinating technological challenges in engineering, since the presence of continuous, intertwined internal channels inaccessible from the outside makes the use of conventional subtractive techniques such as milling or CNC turning impossible [15]; consequently, their realization is closely tied to Additive Manufacturing (AM) [12], [28]. Depending on the material and the final application, different 3D-printing technologies are used: for metals, powder bed fusion processes such as Selective Laser Melting (SLM) or Laser Powder Bed Fusion (L-PBF) are most common, in which a laser selectively melts very thin layers of metal powder, whereas for polymers and resins techniques such as Stereolithography (SLA) or Selective Laser Sintering (SLS) are employed [18], [13], [28], [27]; for lower-cost or prototyping applications, Fused Deposition Modeling (FDM) is also used, now improved by composite filaments loaded with conductive particles [7]. In the field of heat transfer, the most commonly used materials include aluminum alloys such as AlSi10Mg, appreciated for their good compromise between thermal conductivity, lightweight, and manufacturability, copper and its alloys, which offer excellent thermal performance but are more difficult to print due to their high reflectivity, and stainless steels or titanium alloys, selected for applications in extreme conditions. A key advantage of TPMS, especially in sheet configurations, is their self-supporting nature due to continuous curvature without sharp edges, which makes it possible to avoid internal supports during printing, a crucial aspect since such supports would not be removable; however, manufacturing still presents important issues, including the fragility of thin walls, which are susceptible to deformation due to thermal gradients, and geometric deviations caused by over-melting, leading to real thicknesses larger than the CAD model and therefore to a reduction in effective porosity. In addition, freshly printed components always require post-processing. Unfused powder must be carefully removed from internal channels through de-powdering operations, followed by detachment from the base plate, typically by wire electrical discharge machining [6]. A stress-relief heat treatment may be necessary to eliminate residual stresses, stabilize the microstructure, and improve thermal properties. Finally, the high surface roughness due to the "staircase" effect [6] and partially fused powder can increase pressure losses, which is why finishing treatments such as sandblasting or electropolishing are used to reduce roughness and bring the real performance closer to that predicted by numerical models [28], [15].

## 1.3 Aim of the work

This thesis investigates the thermo-hydraulic performance of simplified version of a divertor tile based on Triply Periodic Minimal Surfaces (TPMS), realized through Additive manufacturing (AM). TPMS geometries offer a promising solution for enhancing convective heat transfer while minimizing pressure losses. A key challenge associated with Additive Manufacturing (AM) is the presence of geometric inaccuracies and residual surface roughness, which may affect both hydraulic and thermal behavior. To assess these effects, a validation study was conducted based on experiments performed at Politecnico di Milano. The experimental data were compared with Computational Fluid Dynamics (CFD) simulations, showing good agreement. The numerical results did not require the inclusion of a roughness model, indicating high manufacturing quality with negligible residual roughness. Following validation, simulations were carried out under representative operating conditions. The results demonstrate that the Gyroid TPMS geometry is well suited for high heat flux applications, maintaining solid temperatures below the safety limit of 450°C under both nominal conditions (10 MW/m$^2$) and extreme loads up to 20 MW/m$^2$. Due to the geometric complexity of TPMS structures and the required operating mass flow rates, directly modeling surface roughness would necessitate a high-$y^+$ wall treatment, which in this case is not feasible. Therefore, the effect of roughness was investigated using a set of simplified channel geometries. The roughness model was first verified against analytical solutions for fully developed flow in a circular pipe, and subsequently applied to more complex configurations. Further experimental validation will be required to confirm these findings.

# 2 CFD analysis of manufactured divertor tile with TPMS

## 2.1 Geometry and material

Within the W7-X reactor, the adopted design approach involves the use of modular components, with the objective of realizing a divertor configuration capable of supporting high thermal loads. To more accurately analyze the behavior of each turbulence promoter, simple geometries were considered, allowing the component to be simulated via CFD first and subsequently tested experimentally under the expected thermal load.

For this reason, the sample under analysis was defined with an overall geometry characterized by 100 mm of development along the main flow direction, 25 mm of empty sections respectively at the inlet and outlet, a height of 10 mm, and a width of 50 mm.

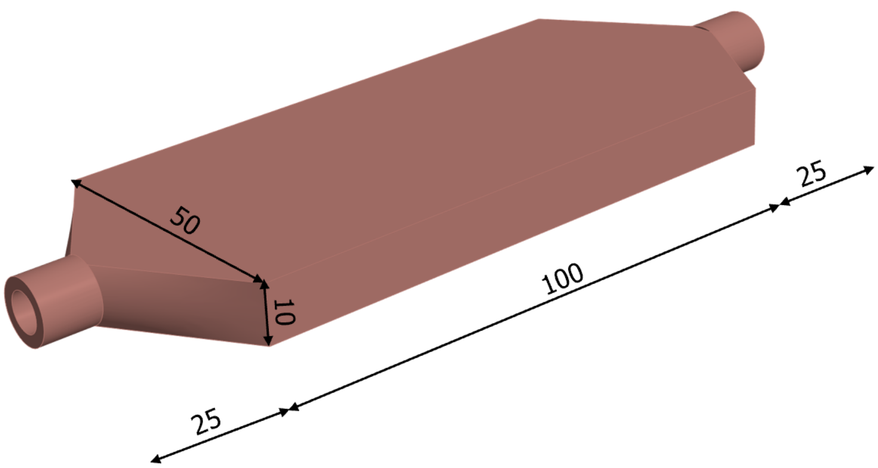


Figure 6: Gyroid sample geometry

As introduced in the previous chapter, the selected turbulence promoter is a TPMS, more specifically a Gyroid-type structure, as shown in the figure. This choice was made in continuity with what is reported in the literature [6], since the Gyroid geometry allows pressure losses to be contained while ensuring a significant increase in the convective heat transfer coefficient. Moreover, it is a configuration that has already been optimized in previous studies [6], making it particularly suitable for the present work.

The TPMS geometry was generated using nTop software [14] and features a unit cell with dimensions of $10 \times 10 \times 5$ mm, with a wall thickness of 1.2 mm. Compared to the geometries adopted in the reference work, an additional precaution was introduced, consisting in shifting the TPMS so that the first channel coincides with the inlet position. This choice was made to further reduce pressure losses.

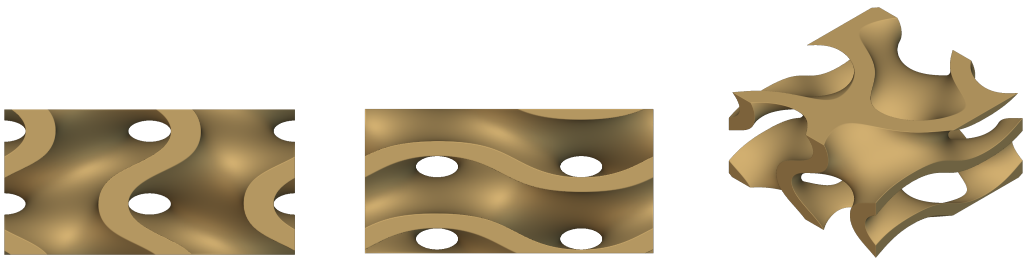

Figure 7: Gyroid adopted for the sample: front, lateral and isometric view

The final configuration of the sample is shown in the cross-sectional figure, where the presence of the TPMS within the structure can be observed.

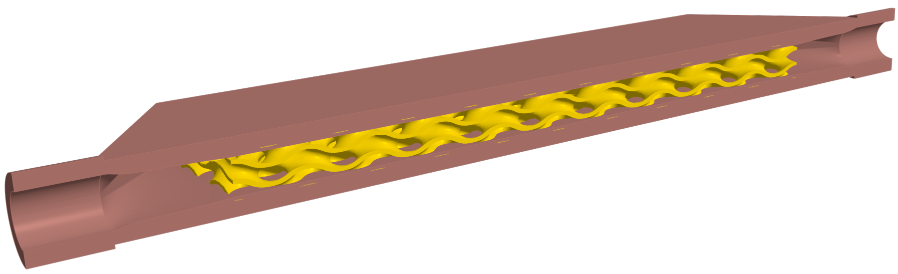

Figure 8: Gyroid sample sectioned

The material used for the sample is CuCrZr, an alloy widely used in the nuclear field due to its ability to withstand high thermal loads. Its thermophysical properties were characterized at the Fraunhofer Center, which also handled the printing of the sample.

Figure 9: CuCrZr gyroid sample [29]

The specimen was fabricated with a surface roughness of 30 $\mu$m and was subsequently subjected to a heat treatment. This treatment consists in maintaining the solid material at a specific temperature for a controlled period of time, in order to modify the microstructure and improve the thermal properties. In particular, the treatment resulted in a significant increase in thermal conductivity compared to the initial condition, as highlighted in the reported graph, where it can be observed that the thermally treated CuCrZr exhibits superior performance compared to the untreated material.

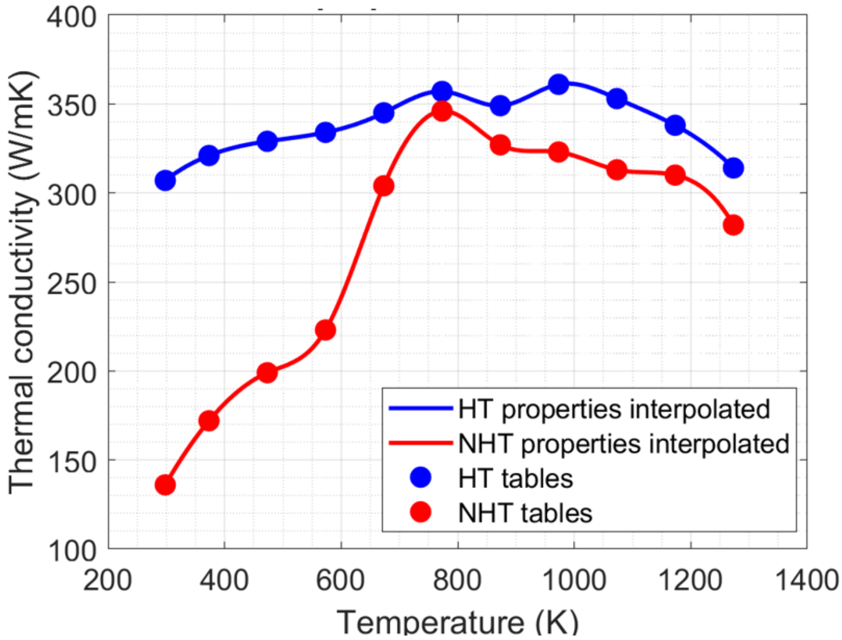


Figure 10: CuCrZr thermal conductivity

## 2.2 Simulation setup

The CFD simulations were carried out using the STAR-CCM+ software [30]. The simulation setup employs a Gyroid-type TPMS structure, as previously introduced, characterized by a unit cell size of $10 \times 10 \times 5$ mm and a wall thickness of 1.2 mm. In order to ensure fully developed flow conditions, additional fluid extrusion regions were included at both the inlet and outlet, with lengths of 50 mm and 25 mm, respectively. This allows the flow to properly develop upstream and downstream of the region of interest.

The working fluid is water, with an inlet temperature of 30°C and a reference pressure of 10 bar. In the initial set of simulations, a progressively increasing mass flow rate was imposed in order to investigate the variation of thermo-hydraulic performance as a function of turbulence intensity.

Given that the nominal mass flow rate for the tile geometry is 0.5 kg/s, corresponding to a Reynolds number of approximately 7000, the Reynolds number was varied in the range of about 2000 to 11000.

For the High Heat Flux (HHF) simulations, the hydraulic limit of the reference design (W7-X) was maintained, corresponding to 0.01 kg $s^{-1}$ $mm^{-1}$, which results in a total mass flow rate of 0.5 kg/s. The simulations were first conducted using the thermally treated material properties of CuCrZr. In the HHF case, both sets of material properties were considered to highlight the differences in thermal response.

A $k$-$\varepsilon$ turbulence model was adopted, specifically the realizable $k$-$\varepsilon$ formulation with a two-layer approach and low-$y^+$ treatment to accurately resolve the boundary layer.

Finally, a heat flux of 10 MW/$m^2$ was imposed. Additional simulations were carried out with increased heat loads up to 20 MW/$m^2$, in order to assess the thermal response under more severe operating conditions.

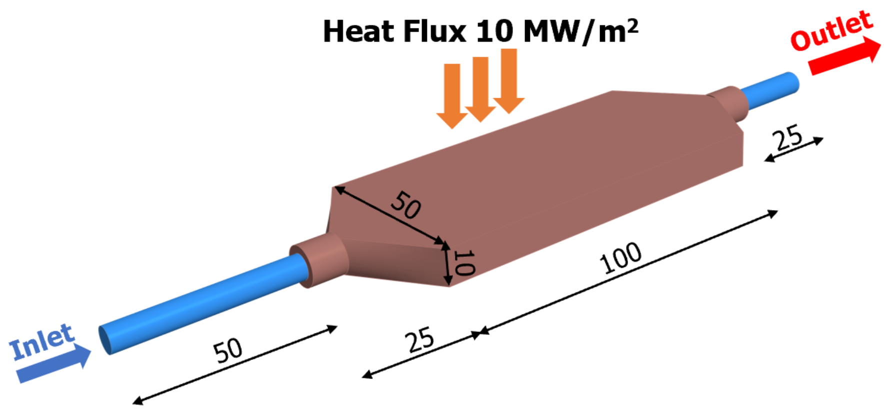


Figure 11: Simulation setup gyroid sample

## 2.3 Models

The models used to solve the thermo-hydraulic problem are distinguished according to the two domains considered, namely the fluid domain and the solid domain. Since the analysis refers to nominal operating conditions, transient phenomena are not considered, and a *steady-state condition* is assumed, in which the fluid is fully developed. In order to reduce the computational cost, a *segregated approach* was adopted instead of a coupled one. This choice is motivated by the well-known mathematical difficulty associated with the pressure-velocity coupling in the solution of the incompressible Navier-Stokes equations. Since pressure does not appear directly in its own transport equation, a Poisson equation for pressure must be solved together with the momentum equation.

The segregated approach reduces computational complexity by means of an alternating and sequential solution of the governing equations: the pressure equation is solved alternately with the momentum equation within iterative cycles defined as outer iterations. In the case of a coupled approach, instead, the pressure Poisson equation and the momentum equation are solved simultaneously, with all unknowns updated at the same computational step.

Since the working fluid is water subjected to high thermal loads, the *IAPWS-IF97* tables were adopted, with temperature-dependent properties. In relation to the mass flow rate under investigation, turbulence was modeled using the Reynolds-Averaged Navier-Stokes (*RANS*) approach, which includes the following governing equations:

$$\nabla \cdot (\rho \vec{v}) = 0 \tag{10}$$

$$\rho \vec{v} \cdot \nabla \vec{v} = -\nabla p + \nabla \cdot [(\mu + \mu_t) \nabla \vec{v}] \tag{11}$$

$$\nabla \cdot (\rho \vec{v} h) = \nabla \cdot \left( \frac{\lambda + \lambda_t}{c_p} \nabla h \right) \tag{12}$$

$$\lambda_s \nabla^2 T = 0 \tag{13}$$

where:

- $\mu_t$ is the turbulent viscosity;
- $c_p$ is the specific heat;
- $\lambda$ and $\lambda_s$ are the thermal conductivities of the fluid and the solid;
- $p$ is the fluid pressure;
- $h$ is the specific enthalpy;
- $T$ is the temperature.

The model adopted for the closure of the RANS equations was the *Realizable* $k-\varepsilon$ *two-layer* model with a *low* $y^+$ approach, since it has been shown in the literature [10] that this model reproduces hydraulic results more accurately than the $k$-$\omega$ SST model under the investigated conditions. The Realizable $k-\varepsilon$ model is a variant of the standard model, developed to overcome its limitations in complex flows. It retains the same transport equation for the turbulent kinetic energy $k$ as the standard model, while introducing an improved formulation for the dissipation rate $\varepsilon$ and a variable turbulent viscosity.

This formulation allows a more accurate prediction of plane and circular jet spreading, improved accuracy in boundary layers subjected to strong adverse pressure gradients or separation, and a better description of flows dominated by rotation, recirculation, and strong curvature of the streamlines.

The Two-Layer treatment also provides a more robust and grid-independent approach, with improved numerical stability for resolving the wall region.

The objective is to extend the solution all the way to the wall by placing the first grid node directly inside the viscous sublayer. To avoid stability issues, the boundary layer is mathematically divided into two distinct regions: a fully turbulent region and a viscous region near the wall. In the first region, far from the wall, the standard $k - \varepsilon$ model is used, where the turbulent viscosity $\mu_{t,t}$ is calculated as:

$$\mu_{t,t} = \rho C_\mu \frac{k^2}{\varepsilon} \tag{14}$$

In the viscous region, only the transport equation for the turbulent kinetic energy $k$ is solved, while the dissipation rate $\varepsilon$ and the turbulent viscosity $\mu_{t,v}$ are prescribed algebraically through a length scale $l$, according to the following expressions:

$$l = \kappa y \left(1 - \exp\left(-\frac{Re_y}{A}\right)\right) \tag{15}$$

$$\varepsilon = \frac{C_\mu^{3/4} k^{3/2}}{l} \tag{16}$$

$$\mu_{t,v} = \rho C_\mu^{1/4} \sqrt{k} l \tag{17}$$

where $\kappa$ is the von Kármán constant and $A$ is set to 70.

To avoid numerical instabilities caused by discontinuities in the calculated turbulent viscosity between the outer region $\mu_{t,t}$ and the inner region $\mu_{t,v}$, a blending function is used. The effective turbulent viscosity throughout the domain is therefore defined as:

$$\mu_t = F_\mu \mu_{t,t} + (1 - F_\mu)\mu_{t,v} \tag{18}$$

where the blending function $F_\mu$ is designed to be zero exactly at the wall and to smoothly approach 1 as the fully turbulent region is reached.

Finally, two additional numerical models were introduced to improve the efficiency and quality of the solution depending on the mesh used: *solution interpolation*, for the fluid region, and *cell quality remediation*, for the solid domain. The former transfers solution fields from a previous mesh to a new one, allowing the computation to restart from an initial field already consistent with the physics of the problem rather than from homogeneous initial conditions. This reduces the number of iterations required to return to a stable convergence region and allows previously computed information to be reused on a different cell topology. The cell quality remediation, on the other hand, acts on the numerical behavior of the solver when the mesh contains low-quality cells, making the calculation more robust and limiting the impact of these problematic control volumes on gradients and residuals.

The final models adopted for the simulations were the following:

| **Fluid domain** | **Solid domain** |
|---|---|
| Three dimensional | Three dimensional |
| Steady | Steady |
| Liquid | Solid |
| Segregated flow | Segregated solid energy |
| IAPWS-IF97 | Polynomial density |
| Segregated fluid temperature | Cell quality remediation |
| Turbulent | |
| RANS | |
| $k-\varepsilon$ turbulence model | |
| Realizable $k-\varepsilon$ two-layer | |
| Two-layer all $y^+$ wall treatment | |
| Solution interpolation | |

Table 1: Models adopted for the gyroid sample

## 2.4 Mesh generation

The choice of the mesh plays a fundamental role in the setup of a CFD model for two main reasons: the accuracy of the results and the computational cost. Achieving an optimal balance between these aspects requires a grid independence study. In this work, a Grid Convergence Index (GCI) analysis was performed, as described in the Appendix, allowing the identification of a mesh that ensures both convergence and reliable results.

For the generation of different meshes, only the base size and prism layer parameters were modified, while all other parameters were kept at their default values. This approach simplifies the grid independence study by focusing on the most influential parameters. Initially, a sensitivity analysis on the base size was carried out using a default number of prism layers in order to identify the optimal resolution. Subsequently, once the base size was fixed, the number of prism layers was varied. This procedure ensured residuals below $10^{-3}$ and, based on a GCI analysis conducted on five meshes with monotonic behavior (and calculated on three grids), the estimated uncertainties were 1.87 % for the pressure drop and 2.69 % for the temperature.

From a computational standpoint, the mesh was divided into two distinct regions corresponding to the analyzed domains: the fluid region and the solid copper region. A low-$y^+$ approach was adopted, with a target value of $y^+ \approx 1$, as shown in the corresponding figure. To achieve this, a first layer thickness near the wall of $5 \times 10^{-3}$ mm was imposed, with a total of 10 prism layers and an overall thickness of 0.4 mm. This approach allows direct resolution of the boundary layer without the use of wall functions.

Prism layers were applied exclusively in the fluid region, as their primary purpose is to resolve the turbulent boundary layer; therefore, they are not required in the solid region, where they were deactivated. Regarding the volume discretization, a polyhedral mesh was adopted, characterized by minimum and maximum base sizes. The selected values were 0.8 mm for the fluid region and 2.4 mm for the solid region. A coarser mesh was used in the solid domain since a high cell density is not required, whereas a finer resolution is necessary in the fluid region, which represents the most computationally demanding part of the problem.

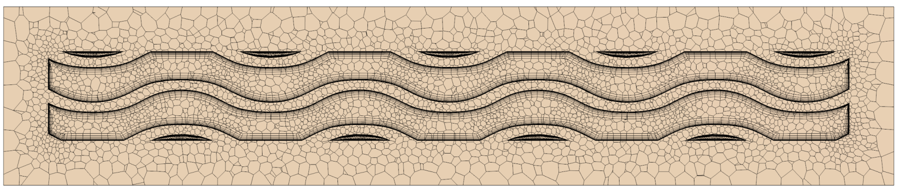

Figure 12: Mesh generation result of gyroid sample

As described in the previous section, two extrusion regions were also introduced at the inlet and outlet to ensure fully developed flow conditions. To reduce the computational cost in these regions, a base size of 2.4 mm was adopted for the extruded fluid portions as well.

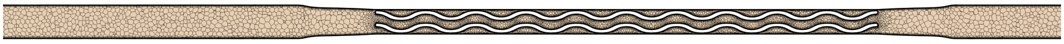

Figure 13: Mesh generation result of the fluid

| **Mesh parameter** | **Region** | | |
|---|---|---|---|
| | **Fuid** | **Solid** | **Inlet/Outlet extrusions** |
| Base size (mm) | 0.8 | 2.4 | 2.4 |
| Surface grow rate | 1.3 | 1.3 | 1.3 |
| Prism layer number | 10 | / | 10 |
| Prism layer near wall thickness (mm) | 5.0e-3 | / | 5.0e-3 |
| Prism layer total thickness (mm) | 0.4 | / | 0.4 |

Table 2: Mesh parameters summary gyroid sample

## 2.5 Results and discussion

### 2.5.1 Post-processing setup

Regarding post-processing, two different types of analyses and graphical representations were considered. In the first case, the behavior of the friction factor and the Nusselt number was evaluated as a function of velocity, and therefore of the Reynolds number and turbulence regime. In the second case, a heat flux test was performed by applying $10\text{MW/m}^2$ heat flux and assessing up to which value the sample remains under safe operating conditions. To this end, the heat flux was increased up to $20\text{MW/m}^2$.

The above-mentioned parameters were calculated using the following relations.

For the evaluation of the heat transfer coefficient (HTC), the following expression was used:

$$HTC = \frac{\text{heat flux}}{T_{\text{wall}} - T_{\text{bulk, fluid}}} \tag{19}$$

In this expression, $T_{\text{wall}}$ represents the surface-averaged temperature of the wetted wall, while $T_{\text{bulk,fluid}}$ denotes the mass-flow-averaged fluid temperature, evaluated at the outlet of each region highlighted in red in the figure.

Figure 14: Heat Transfer Coefficient regions

Subsequently, the HTC was evaluated locally on four different sections within the fully developed region. The overall heat transfer coefficient was then obtained by applying an arithmetic mean of these four local values, in order to ensure a more accurate estimation.

For the identification of the fully developed region, a criterion available in the literature for TPMS structures was adopted: generally, the flow is considered fully developed after 2–3 unit cells. In the present case, the fully developed region starts approximately 20 mm downstream of the TPMS inlet.

Regarding the friction factor was calculated using the Darcy-Weisbach correlation:

$$f = \frac{2 \cdot \Delta p \cdot D_h}{\rho \cdot L \cdot v^2} \tag{20}$$

In this relation, $\Delta p$ represents the pressure drop, $D_h$ the hydraulic diameter, $\rho$ the fluid density, $L$ the channel length, and $v$ the mean fluid velocity.

Finally, the Nusselt number was calculated using a correlation combining the HTC, the hydraulic diameter, and the thermal conductivity of the fluid was adopted:

$$Nu = \frac{HTC \cdot D_h}{k} \tag{21}$$

The choice of using the Nusselt number, the friction factor, and the Reynolds number is motivated by the use of dimensionless quantities, which allow a direct correlation between thermal and hydraulic behavior, making the analysis independent of the measurement units.

### 2.5.2 Nusselt & friction factor vs flow speed

The first aspect analyzed in the CFD simulations concerns the thermo-hydraulic behavior of the sample as a function of turbulence, which is varied by modifying the fluid velocity. As shown in the figure below, it is clearly observed that the Nusselt number increases with increasing Reynolds number. This behavior is due to the thinning of the thermal boundary layer at the wall, which enhances heat transfer between the fluid and the wall and increases the heat transfer coefficient.

Moreover, the presence of turbulence promoters generates vortical structures even at low velocities, enhancing heat transfer; as the velocity increases, these vortices become more intense, further improving convective heat transfer. This confirms a strong thermo-hydraulic coupling: an increase in the heat transfer efficiency in the fluid directly leads to a reduction in the solid temperature.

Regarding the friction factor, it is observed that as the velocity increases, it initially decreases until reaching a minimum value, and then increases again. This behavior is typical of certain porous media or complex geometries, where, beyond a certain Reynolds number, inertial effects become dominant and lead to an increase in pressure losses.

In all the simulations considered, the heat flux was kept constant at $10\,\mathrm{MW/m^2}$, while the Nusselt number was calculated according to the methodology described in the previous section.

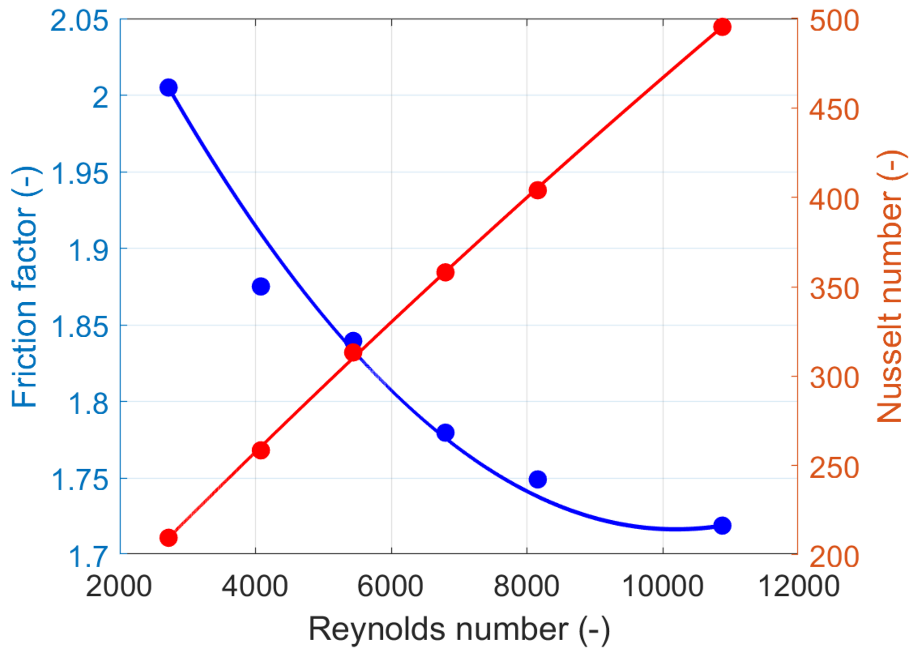


Figure 15: Nusselt number and friction factor vs flow speed

### 2.5.3 W7-X operating condition: High Heat Flux test (HHF)

The High Heat Flux (HHF) test will be performed at the Forschungszentrum Jülich research center, where the pressure drop will be measured under a prescribed mass flow rate of 0.5 kg/s. The surface heat flux will be applied by means of an electron beam gun with a maximum power of 200 kW, increasing the power density stepwise in increments of 1 MW/m$^2$ until the target heat load is reached and a steady-state thermal condition is attained. In parallel, the temperature of the heated surface will be monitored using infrared cameras, while a graphite layer, owing to its low emissivity, is used to reduce measurement noise and improve the quality of the thermal acquisition. The applied heat load will range from 10 MW/m$^2$ to 20 MW/m$^2$, representing the worst-case scenario under disruption conditions. In this section, CFD simulations are carried out to predict the performance of the tile under the experimental conditions described above, pending the test campaign scheduled for the end of 2026.

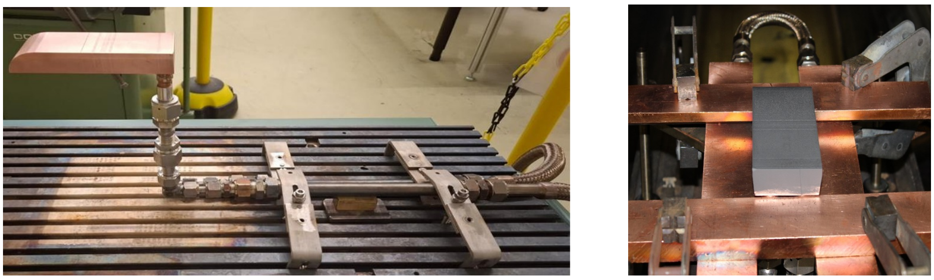

Figure 16: High Heat Flux test (HHF) experimental setup [31]

#### Simulation results

The specimen exhibited a pressure drop of 2.67 bar, well below the limit of 10 bar accepted by the water circuit. The pressure streamlines are shown in Figure 17.

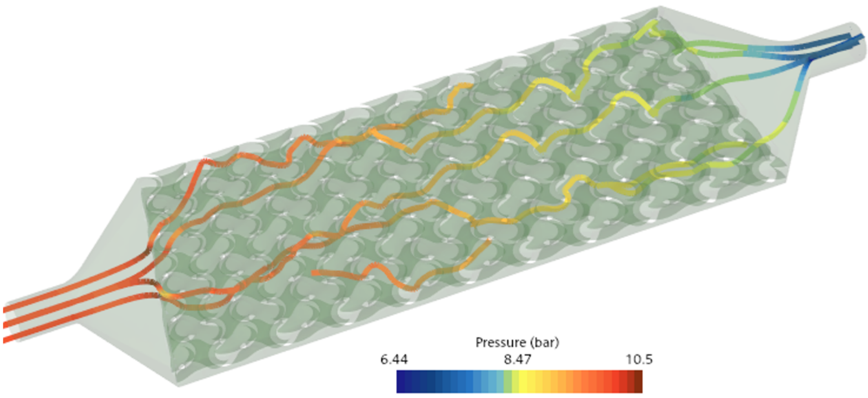


Figure 17: HHF fluid pressure drop

As explained previously, both the thermally treated CuCrZr specimen and the untreated one were simulated. In the thermally treated case, it can be observed that the temperature is lower due to the higher thermal conductivity. Considering that the saturation temperature of water at 10 bar is 179.9°C, it can be noted that boiling will occur at some contact points near the inlet section, future works will implement optimization of such regions to prevent boiling also here.

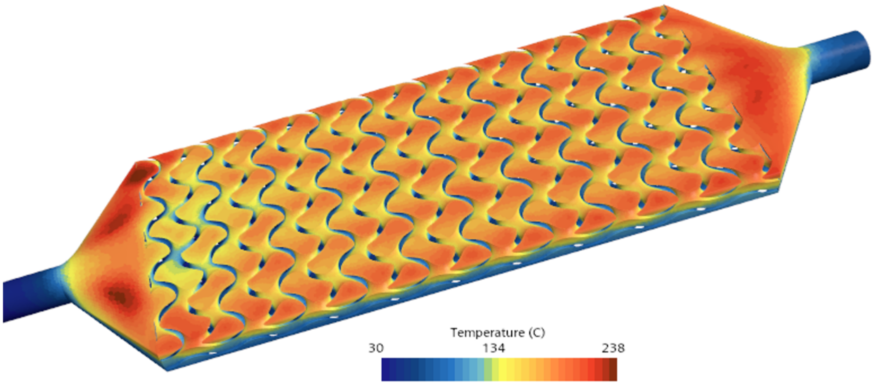


Figure 18: HHF fluid temperature with heat treated CuCrZr

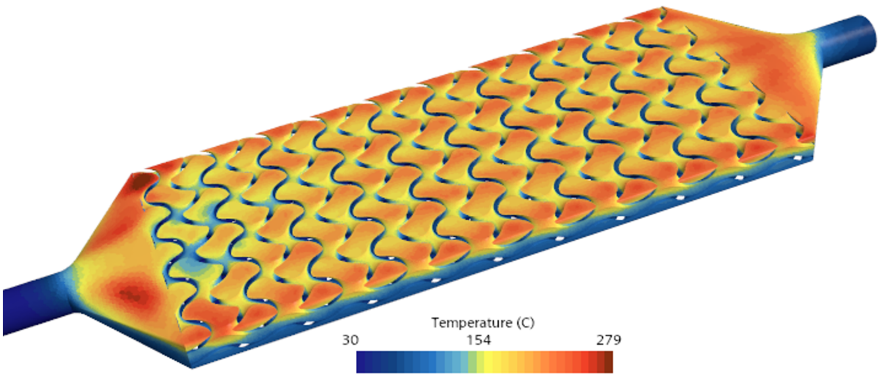


Figure 19: HHF fluid temperature with non heat treated CuCrZr

In the following figures, the thermal response of the solid can be observed. As expected, the maximum temperature of the thermally treated specimen is lower than that of the untreated one. In both cases, however, the temperature remains below the thermal limit of CuCrZr, which is approximately 450°C. It should also be noted that the actual solid temperature may be slightly higher in regions where boiling occurs; therefore, a boiling model should be implemented in future work to account for this effect. Regarding the temperature distribution along the specimen, it can be observed that it is asymmetric, which is due to the fact that the specimen itself is not symmetric.

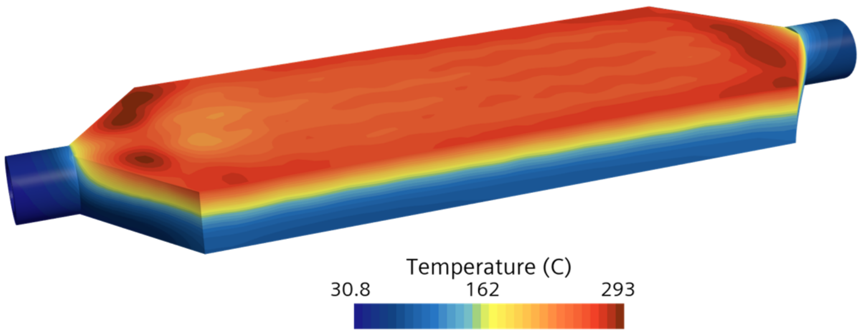


Figure 20: HHF solid temperature with heat treated CuCrZr

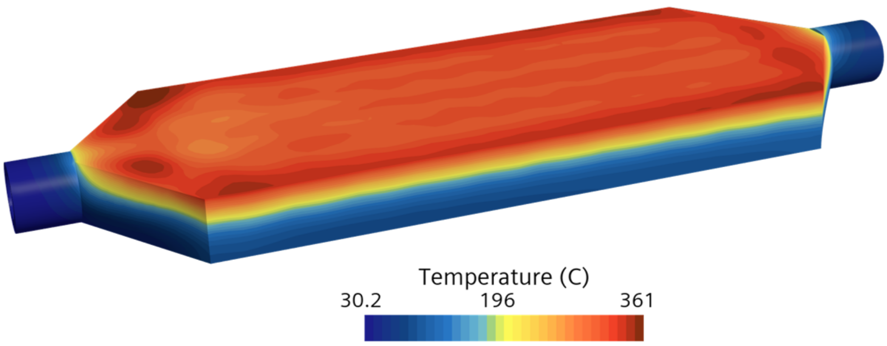


Figure 21: HHF solid temperature with non heat treated CuCrZr

As summarized in the following table, the main results of these simulations are presented. From these simulations, it emerges that thermally treated CuCrZr is a recommended processing method because it allows for lower temperatures in the specimen.

| | **HT CuCrZr** | **NON HT CuCrZr** |
|---|---|---|
| Pressure drop $\Delta p$ (bar) | 2.67 | 2.67 |
| Maximum fluid temperature $T_{max,fluid}$ (°C) | 238 | 279 |
| Maximum solid temperature $T_{max,solid}$ (°C) | 294 | 361 |

Table 3: HHF summary results

Additional simulations were then performed by keeping the mass flow rate constant at 0.5 kg/s, consistently with the mass flow rate limit available for the divertor, while increasing the thermal load up to 20 MW/m$^2$ to consider more extreme loading conditions. For the fully developed region, a distance of approximately two unit cells (20 mm) was considered, beyond which the fluid can be regarded as fully developed.

The solid temperature was calculated as an average over the heated solid surface, computed every 2.5 mm. Considering that the safety limit of CuCrZr is approximately 450°C, it can be observed that for all five simulated thermal loads, the temperature remains below this limit, reaching a maximum temperature of approximately 370°C at 20 MW/m$^2$.

In the graph below, the first minimum is due to the fact that water enters through an empty pipe before entering the region constituted by the TPMS and requires approximately 20 mm to develop; beyond this point, the fully developed region begins, with the expected temperature increase as reported in the literature.

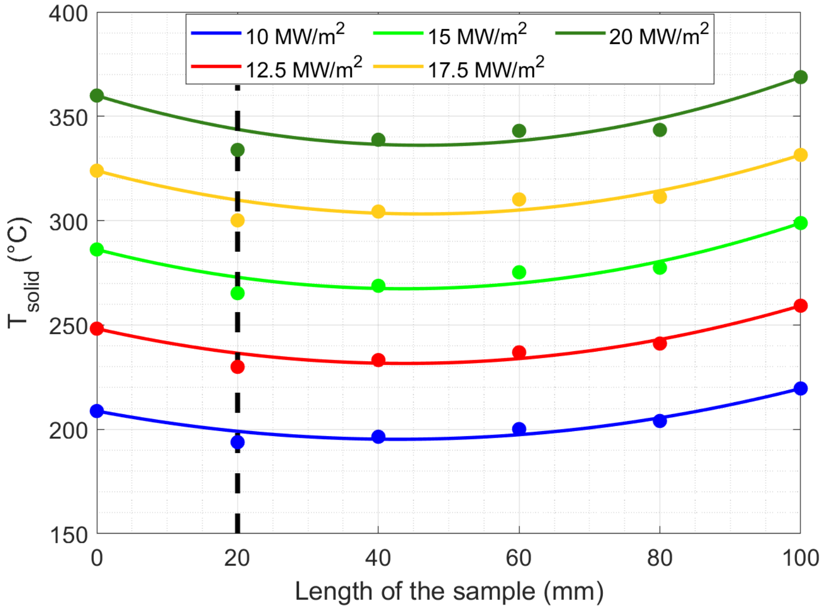


Figure 22: HHF solid temperature changing the heat flux

### 2.5.4 Validation

In order to assess the reliability of the numerical solutions obtained from the CFD simulations, the specimen previously analysed was experimentally characterised at a laboratory of the Politecnico di Milano. The test section is connected to the hydraulic loop through two junctions leading to the pressure transducer; in the vicinity of the sensor, safety valves are installed to protect the system in the event of overpressure. The loop is driven by a pump and includes a manual control valve used to adjust the mass flow rate, which is measured by means of a Coriolis mass flow meter. Data acquisition was performed electronically using LabView [32], with a sampling frequency of 1 Hz. The instrumentation employed in the experimental campaign is summarised in Table 4.

To exclude the initial transient associated with plant stabilisation, only the last 3 min of each test were retained for post-processing. At a sampling

| Instrument | Model / Note | Range | Accuracy |
|---|---|---|---|
| Pump | B-NMD 25/190AE-60 | 0–9600 kg $h^{-1}$ | – |
| Mass flow meter | – | 0–6500 kg $h^{-1}$ | 3% FS |
| Pressure transducer | – | 0–100 kPa | 0.2 kPa |

Table 4: Instrumentation used in the experimental validation campaign.

rate of 1 Hz, this corresponds to $N = 180$ samples:

$$N = 3 \times 60 \times 1 = 180. \tag{22}$$

The mean mass flow rate, $Q$ [kg $h^{-1}$], was computed as the arithmetic average of the samples acquired from the flow meter channel:

$$Q = \frac{1}{N} \sum_{i=1}^{N} Q_i. \tag{23}$$

The mean differential pressure drop, $\Delta P$ [Pa], was obtained from the pressure transducer signal by subtracting the hydrostatic and atmospheric offset of the facility, equal to 60 kPa, and converting the result into SI units:

$$\Delta P = \left( \frac{1}{N} \sum_{i=1}^{N} \mathrm{RSPD04}_i - 60.0 \right) \times 1000. \tag{24}$$

The uncertainty bars shown in the final comparison were determined by combining the statistical uncertainty associated with the measured fluctuations and the instrumental uncertainty provided by the sensor specifications. For the mass flow meter, the stated accuracy is 0.2% of the full scale, corresponding to a maximum instrumental error of

$$\Delta_{\mathrm{instr}} = 0.002 \times FS = \pm 0.8 \text{ kg h}^{-1}, \tag{25}$$

where $FS = 400$ kg $h^{-1}$. Assuming a rectangular probability distribution, the corresponding standard uncertainty is

$$u_{\mathrm{instr}} = \frac{\Delta_{\mathrm{instr}}}{\sqrt{3}} \approx 0.462 \text{ kg h}^{-1}. \tag{26}$$

The statistical contribution was estimated from the standard deviation of the steady-state signal:

$$u_{\mathrm{stat}} = \frac{\sigma_Q}{\sqrt{N}}. \tag{27}$$

The combined standard uncertainty of the mean mass flow rate was therefore expressed as

$$u_{c,Q} = \sqrt{\left(\frac{\sigma_Q}{\sqrt{N}}\right)^2 + \left(\frac{\Delta_{\mathrm{instr}}}{\sqrt{3}}\right)^2}. \tag{28}$$

Assuming a coverage factor $k = 2$, which approximately corresponds to a 95% confidence level, the expanded uncertainty becomes

$$U_Q = 2\, u_{c,Q}. \tag{29}$$

For the differential pressure, the uncertainty of the mean was evaluated as

$$u_{c,\Delta P} = \frac{\sigma_{\Delta P}}{\sqrt{N}}, \tag{30}$$

and the corresponding expanded uncertainty was obtained as

$$U_{\Delta P} = 2\, \frac{\sigma_{\Delta P}}{\sqrt{N}}. \tag{31}$$

In turbulent flow conditions, the pressure drop across the channel is expected to follow a quadratic dependence on the mass flow rate. Accordingly, the experimental data were fitted with the model

$$\Delta P = a\, Q^2, \tag{32}$$

where $a$ is the hydraulic coefficient to be identified.

The coefficient $a$ was obtained through a least-squares regression by minimising the objective function

$$S(a) = \sum_{j=1}^{m} \left(\Delta P_j - a\, Q_j^2\right)^2. \tag{33}$$

By imposing the first-order optimality condition, $\partial S/\partial a = 0$, the analytical solution is obtained as

$$a = \frac{\sum_{j=1}^{m} Q_j^2 \Delta P_j}{\sum_{j=1}^{m} Q_j^4}. \tag{34}$$

Since the regression model is constrained to pass through the origin, the goodness of fit was evaluated through the uncentered coefficient of determination:

$$R^2 = 1 - \frac{\sum_{j=1}^{m} \left(\Delta P_j - \hat{\Delta P}_j\right)^2}{\sum_{j=1}^{m} \left(\Delta P_j\right)^2}, \tag{35}$$

where $\hat{\Delta P}_j = aQ_j^2$ is the fitted value.

Figure 23 compares the experimental measurements with the CFD predictions. The experimental points are shown together with their uncertainty bands, while the numerical values are superimposed for direct comparison. The agreement between the two sets of results confirms the consistency of the numerical model.

Looking at Figure 23, the numerical results are in good agreement with the experimental data. This suggests that the specimen exhibits very limited roughness, consistent with the high quality of the manufacturing process, and that no significant additional pressure losses are introduced. Accordingly, the High Heat Flux simulations presented in Section 2.5.3 can now be regarded as a reliable representation of the actual behavior of the system.

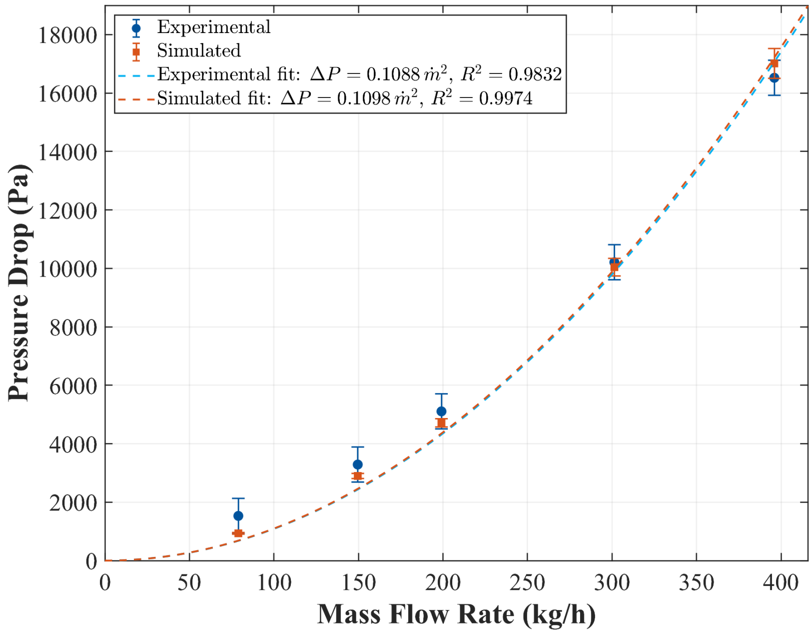


Figure 23: Comparison between experimental measurements and CFD predictions.

# 3 Effect of roughness

## 3.1 Geometry and material

In order to properly assess the effect of surface roughness in Star-CCM+, it is necessary to adopt a high $y^+$ approach, so as to correctly employ the roughness model implemented in the software (described in greater detail in the following subsections). However, given the considered flow rates and the geometric complexity typical of TPMS structures, this condition is difficult to achieve. Although theoretically feasible, it would require a significant increase in turbulence levels, leading to very high flow rates that are difficult to reproduce experimentally.

To overcome these limitations, experimental specimens manufactured at the Max Planck Institute for Plasma Physics (IPP) in Greifswald were adopted [33]. These samples were produced via additive manufacturing using the same technology and supplier employed for the gyroid specimen. All specimens share a common configuration: a copper plate, on which the heat flux is imposed, is bonded to a CuCrZr solid block, within which the fluid channel is embedded.

The thermophysical properties of the solid material are the same as those described in the previous chapter for the gyroid specimen; however, in this case, the heat-treated state was directly considered, since the manufactured samples underwent such treatment. Geometrically, each specimen has dimensions of 6 mm in width (except var5.1 which is 1mm larger), 8 mm in height, and 100 mm in length, while the copper plate has a thickness of 1 mm.

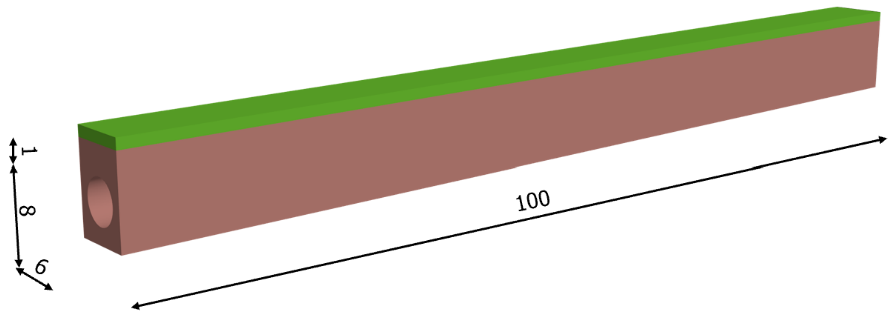


Figure 24: Geometry design for the study of roughness

The differences among the configurations lie both in the channel shape and in the presence and type of internal turbulence promoters, designed to induce vortical structures and enhance convective heat transfer. The same specimens were also independently simulated by the Jožef Stefan Institute (JSI) in Ljubljana, allowing for an additional comparison with the obtained CFD results.

The considered geometries, shown in Figure 25, are as follows: configuration Var1.1 consists of a simple circular pipe without turbulence promoters; Var1.0 features a circular cross-section with an internal swirl; finally, Var5.1 is characterized by a triangular cross-section combined with a swirl, representing the most complex configuration.

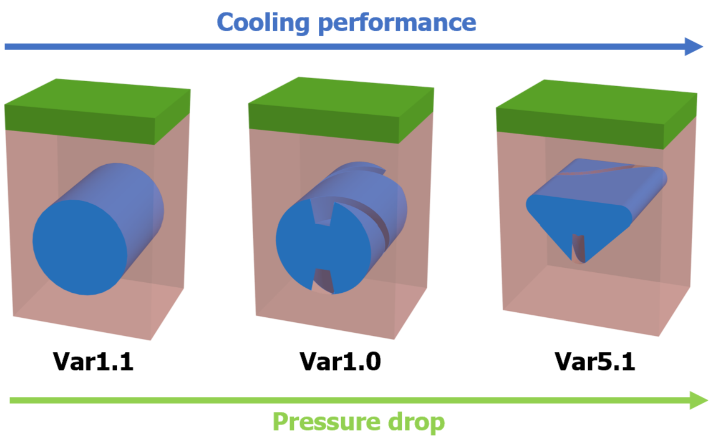


Figure 25: Specimens selected for the study of roughness

As expected, increasing channel complexity leads to improved cooling performance, but also to higher pressure losses. Moreover, for identical external specimen dimensions, variations in internal geometry result in different hydraulic diameters, which decrease from configuration Var1.1 to Var1.0, and further to Var5.1, as reported in the following table.

| **Specimen** | **Hydraulic diameter $\mathbf{D_h}$ (mm)** |
|---|---|
| Var1.1 | 4.00 |
| Var1.0 | 2.40 |
| Var5.1 | 2.04 |

Table 5: Hydraulic diameters of the specimens

## 3.2 Simulation setup

The CFD simulations were carried out using the STAR-CCM+ software [30]. An extension of 50 mm at the inlet and 25 mm at the outlet was added to the original specimen geometry in order to ensure a fully developed flow field.

Water was used as the working fluid at a temperature of 30 °C and a reference pressure of 10 bar. The mass flow rate was defined according to the hydraulic limit of the W7-X reactor, equal to 0.01 kg/s·mm, resulting in a total mass flow rate of 0.06 kg/s. The heat flux imposed on the copper plate was set to 10 $MW/m^2$, corresponding to the expected peak heat flux within the reactor that can interact with the divertor. These operating conditions were also selected in view of the experimental campaigns planned for the analyzed specimens, as described in the previous chapter.

Each simulation was first performed considering a smooth channel and subsequently repeated by introducing a roughness model with specific parameters, assuming a roughness height of 60 $\mu$m, in order to reproduce the behavior of the rough channel.

All cases were simulated using the k-$\omega$ SST turbulence model. The boundary layer was modeled using a high $y^+$ approach, as this formulation is required by the software for the application of the roughness model.

The main simulation characteristics and the corresponding boundary conditions are summarized in the following figure and table.

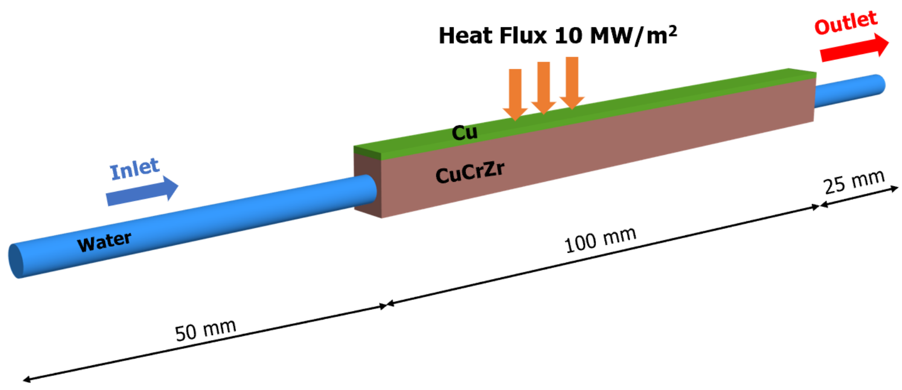


Figure 26: Simulation setup for roughness specimen

| Boundary conditions | |
|---|---|
| Work fluid | Water |
| Mass flow rate | 0.06 $kg/s$ |
| Inlet temperature | 30 $°C$ |
| Reference pressure | 10 bar |

Table 6: Boundary conditions summary for roughness specimens

## 3.3 Models

The numerical framework adopted in this work is consistent with that described in the previous section, with the only difference being the turbulence closure model used in the present simulations. The fluid and solid domains are both treated as three-dimensional steady-state problems, and the solution strategy remains segregated. The thermophysical properties of water are still described through the IAPWS-IF97 formulation, while the solid region is modelled by means of a polynomial density law. In addition, the same general treatment of the solid energy equation and the same numerical framework for the coupled thermo-hydraulic problem are retained.

In the present case, the turbulence was modelled using the $k$-$\omega$ SST approach with an all-$y^+$ wall treatment. This choice was made in order to remain consistent with the modelling strategy adopted by JSI, so as to enable a direct and meaningful comparison between the two sets of results. The remaining modelling assumptions were left unchanged, since the objective of this study was not to compare different turbulence closures, but rather to assess the influence of the specimen geometry and of the roughness modelling under the same reference framework. This approach allows the comparison to focus on the differences arising from the physical configuration, instead of being affected by variations in the numerical setup.

| **Fluid domain** | **Solid domain** |
|---|---|
| Three-dimensional | Three-dimensional |
| Steady-state | Steady-state |
| Liquid | Solid |
| Segregated flow | Segregated solid energy |
| IAPWS-IF97 | Polynomial density |
| Segregated fluid temperature | Cell quality remediation |
| Turbulent | |
| RANS | |
| $k$-$\omega$ SST turbulence model | |
| All-$y^+$ wall treatment | |
| Solution interpolation | |

Table 7: Models adopted for roughness simulations

## 3.4 Roughness model

Surface imperfections, in the field of fluid dynamics, can significantly alter the velocity field and change the flow behavior inside a specimen. Since roughness almost always has dimensions that are too small to be resolved and directly modeled by the mesh, the use of specific models is therefore required. In general, the effect of roughness is modeled by shifting the internal boundary-layer logarithmic layer (*log layer*) closer to the wall.

Figure 27 shows the behavior of the dimensionless velocity profile near a wall and, in particular, illustrates the mathematical issue that arises when applying the roughness model.

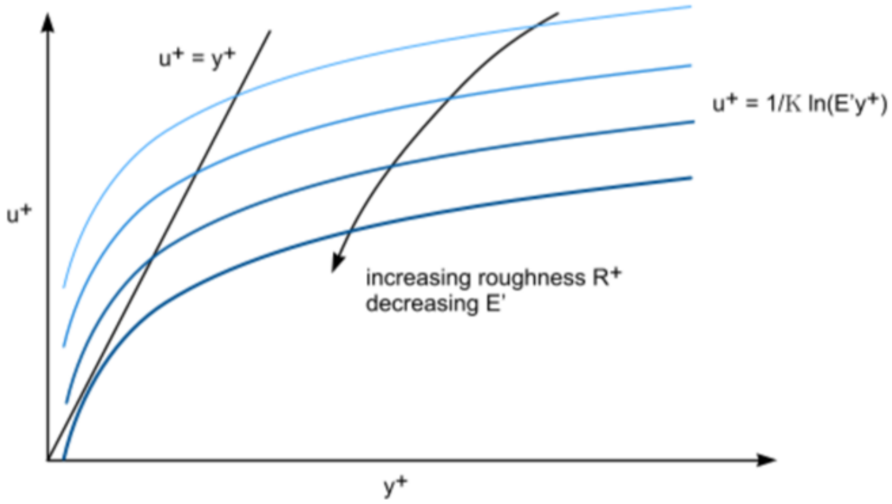


Figure 27: Dimensionless velocity profile near the wall [34]

In this graph, the ordinate represents the dimensionless velocity $u^+$, while the abscissa represents the dimensionless distance from the wall $y^+$. The black straight line, $u^+ = y^+$, represents the linear velocity profile assumed in the viscous sublayer, namely the infinitesimal region of the fluid in direct contact with a smooth wall, while the blue curves represent the velocity profile in the turbulent logarithmic layer (*log-layer*).

As the roughness parameter $R^+$ increases, the term responsible for the curve shift decreases, causing the curves to move downward. The graph shows that this displacement of the logarithmic profile, represented by the blue lines, may prevent intersection with the usual linear profile of the viscous sublayer, represented by the black line. This represents the basic physical concept behind roughness models: the offset of the logarithmic law is reduced and the logarithmic layer of the internal boundary layer is mathematically shifted closer to the wall.

Simcenter STAR-CCM+ [34] handles this anomaly depending on the flow regime. In the fully rough regime, if the lack of intersection occurs, there is no mathematical or physical issue because the viscous sublayer is considered entirely irrelevant. In the transitional roughness regime, if the curves do not intersect during the transition phase, the software still uses the logarithmic profile for calculations, but with an essential safety constraint: the velocity value is never allowed to fall below zero.

This distinction is made by defining a roughness parameter $R^+$, which is computed as

$$R^+ = \frac{r\rho u_*}{\mu} \tag{36}$$

where:

- $r$ is the equivalent sand-grain roughness height;
- $\rho$ is the fluid density;
- $u_*$ is the velocity scale;
- $\mu$ is the dynamic viscosity.

The methods used by the software to solve the rough wall problem are of two types and differ according to how the boundary layer problem is treated:

the Rough model and the Rough Displaced Origin model.

The Rough model uses coefficients to define a roughness function $f$, in order to minimize the displacement $E$ in the log-law by modifying the wall functions for velocity and temperature. The model can be described by the following expression:

$$f = \begin{cases} 1 & ; \quad R^+ \leq R^+_{smooth} \\ \left[ B \left( \dfrac{R^+ + R^+_{smooth}}{R^+_{rough} - R^+_{smooth}} \right) + CR^+ \right]^a & ; \quad R^+_{smooth} < R^+ < R^+_{rough} \\ B + CR^+ & ; \quad R^+ > R^+_{rough} \end{cases} \tag{37}$$

with

$$a = \sin \left[ \frac{\pi}{2} \frac{\log \left( R^+ / R^+_{smooth} \right)}{\log \left( R^+_{rough} / R^+_{smooth} \right)} \right] \tag{38}$$

where $B$ and $C$ are model constants, while $R^+_{rough}$ and $R^+_{smooth}$ are roughness parameters corresponding to the fully turbulent and fully smooth limits, respectively, and are constants.

For the model to work properly, the first layer near the wall must be at least as far from the wall as the roughness being simulated, which introduces a resolution constraint: the model requires a high-$y^+$ approach ($y^+ > 30$). If this condition is not satisfied, the software limits the local roughness and sets it equal to the distance of the first layer from the wall.

The Rough Displaced Origin method, instead, handles the effects of surface imperfections by mathematically shifting the origin of the boundary layer above the roughness height. Unlike the standard model, which only reduces the offset of the logarithmic law, this approach uses dedicated wall functions to recalculate all the main near-wall flow quantities. Specifically, the dimensionless velocity is modeled by combining the origin shift with a modification of Reichhardt's blended law, applying mathematical limits to ensure physically meaningful velocity profiles. In parallel, the dimensionless temperature is computed using a specific blending function, while the turbulent and specific dissipation rates are recalculated to adapt to the various regimes, ultimately including the concept of a "fully rough surface," namely a condition in which the roughness is so high that it completely eliminates the typical viscous flow behavior near the wall.

After a series of simulations, it was found that the Rough method performs better, and it was therefore adopted for the simulations with the rough surface.

The next step was to model coefficients $B$ and $C$ so that they were consistent with the chosen roughness, in this case $60\,\mu$m, and with the hydraulic diameter of Variant 1.1 (a circular channel without turbulence promoters). To do this, an iterative method was chosen in order to obtain these roughness parameters, taking into account that $R^+_{smooth}$ and $R^+_{rough}$ were fixed. First, the physical parameter to be modified was selected, namely the thermal part, the hydraulic part, and the coupled one. Following the simulations, it was observed that the different parameters influence the physical quantities; more specifically, parameter $B$ modifies the thermal part, parameter $C$ the hydraulic part, and both in the case of coupled improvement.

Once the roughness parameter had been chosen, increments were carried out with three mesh refinement levels: coarse, medium, and fine. The reference correlations used were the Gnielinsky correlation for the Nusselt number and the Darcy correlation for the pressure drop. The error between the Nusselt number and pressure drop obtained from the simulation and those from the reference correlations was then computed using the least-squares method, and the increment was continued until the error was decreasing.

The results obtained from the iterative method are reported in the following table. At first glance, the coupled method may seem like a good compromise, but changing the parameters resulted in thermal behavior opposite to what is expected in the literature. For this reason, in the next simulations, separate thermal and hydraulic parameter sets will be adopted to describe the thermal and hydraulic behavior of the specimen, respectively.

| **Roughness model (Var1.1, $\varepsilon = 60\,\mu$m)** | | | |
|---|---|---|---|
| **Method** | **#** | **Correlation** | **Simulated** |
| Hydraulic | $\Delta p$ (bar) | 6.53E-2 | 6.04E-2 |
| | Nu | 234 | 307 |
| Thermal | $\Delta p$ (bar) | 6.53E-2 | 5.94E-2 |
| | Nu | 234 | 234 |
| Coupled | $\Delta p$ (bar) | 6.53E-2 | 7.26E-2 |
| | Nu | 234 | 275 |

| **Thermal** | |
|---|---|
| $R^+_{\text{smooth}}$ | 0.01 |
| $R^+_{\text{rough}}$ | 5.0 |
| $B$ | 3.4658 |
| $C$ | 0 |

| **Hydraulic** | |
|---|---|
| $R^+_{\text{smooth}}$ | 0.01 |
| $R^+_{\text{rough}}$ | 5.0 |
| $B$ | 0 |
| $C$ | 0.30473 |

| **Coupled** | |
|---|---|
| $R^+_{\text{smooth}}$ | 0.01 |
| $R^+_{\text{rough}}$ | 5.0 |
| $B$ | 1 |
| $C$ | 0.17814 |

Table 8: Roughness model parameters

## 3.5 Mesh generation

To correctly apply the roughness model implemented in the software, a high-$y^+$ approach is required for the boundary-layer modelling. Through a series of mesh trials, an initially fully resolved mesh was tested in order to achieve values of $y^+$ much greater than 30 over the entire domain. However, it was observed that, in the first part of the specimen, the fluid is not yet fully developed and exhibits a lower velocity, which leads to values of $y^+$ below 30 or, in some regions, within the buffer layer. To avoid this issue, a hybrid mesh was adopted, allowing the first portion of the specimen to be treated with a low-$y^+$ approach and the subsequent region, starting from $x = 40$ mm, to be modelled with a high-$y^+$ approach, thus ensuring a fully developed region with $y^+ > 30$.

Regarding the general geometric settings, the following mesh parameters were adopted: a base size of 0.22 mm for water, 0.27 mm for CuCrZr, and 0.07 mm for copper, with particular reference to the upper surface of the copper plate on which the heat flux is applied. The surface growth rate was kept equal to 1.3.

As for the prism layers, which are a crucial part of this type of modelling, different parameters were defined for the two computational regions. In the high-$y^+$ region, the first layer adjacent to the wall was set to 0.2 mm, with a total thickness of 0.75 mm and three layers. In the upstream part, modelled with a low-$y^+$ approach, the first layer thickness was set to $1 \times 10^{-5}$ m, with 20 layers, while keeping the total thickness unchanged with respect to the high-$y^+$ region.

Since additional extensions are present near the outlet, the computational cost was reduced by increasing the base size by a factor of 3.5 in that region. The mesh for the specimens was therefore generated with the aim of achieving, as discussed in Chapter 2, an appropriate compromise between numerical accuracy and computational cost. To ensure sufficient reliability of the discretisation, a grid-independence study was also performed in order to verify that the trend of the main physical quantities was monotonic and asymptotic as the characteristic cell size was reduced.

The study was carried out using Richardson extrapolation, as described in the Appendix, thus allowing the final grid to be defined with an estimated accuracy of 0.75% for the pressure drop, 0.18% for the fluid temperature, and 5.30% for the solid temperature.

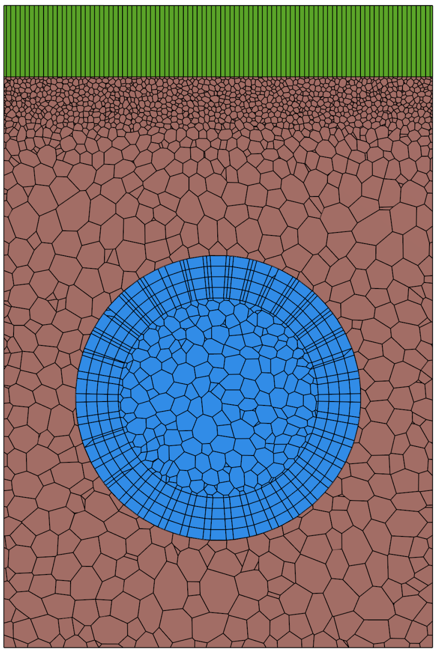

Figure 28: Mesh generation result

| Mesh parameter | Region | | |
|---|---|---|---|
| | **Fuid** | **Solid** | **Inlet/Outlet extrusions** |
| Base size (mm) | 0.22 | 0.27 | 0.33 |
| Surface grow rate | 1.3 | 1.3 | 1.3 |
| Prism layer number | 4 | / | 4 |
| Prism layer near wall thickness (mm) | 0.2 | / | 0.2 |
| Prism layer total thickness (mm) | 0.75 | / | 0.75 |

Table 9: Mesh parameters summary roughness sample

## 3.6 Results and discussion

### 3.6.1 Post-processing setup

Before presenting the results obtained from the CFD simulations, it is necessary to describe the post-processing methodology.

Regarding data extraction, two different approaches were adopted for the fluid and solid regions. In the fluid region, several cross-sectional planes were defined, each spaced 5 mm apart, in order to accurately capture the fluid behavior, also accounting for the presence of turbulence promoters.

For the solid region, data were extracted along a specific line, from which 10000 equally spaced points were sampled.

Based on these data, the following plots were generated to analyze the thermo-hydraulic behavior of the system under a heat flux of 10 MW/m$^2$:

- pressure gradient;
- fluid temperature profile;
- solid temperature profile.

Subsequently, the convective heat transfer coefficient was defined and evaluated on three different cylinders located within the fully developed fluid region, according to the following expression:

$$HTC = \frac{heatflux}{T_{\text{wall}} - T_{\text{bulk,fluid}}} \tag{39}$$

where $T_{\text{wall}}$ represents the surface-averaged temperature of the wetted wall, while $T_{\text{bulk,fluid}}$ is the mass-flow-averaged fluid temperature at the outlet of each region highlighted in red in the figure.

The final value of the heat transfer coefficient was obtained by averaging the values computed over the three cylinders.

Finally, a comparison between the Nusselt number and the friction factor was carried out, considering both smooth and rough wall conditions.

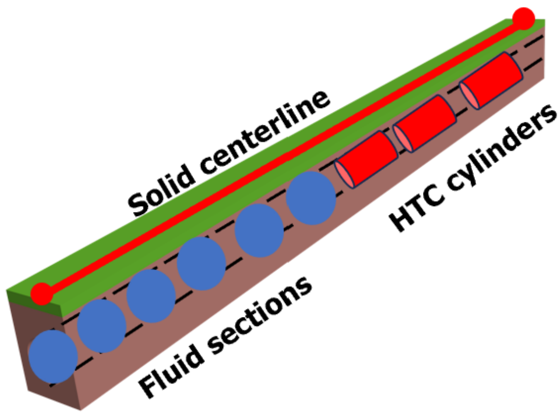


Figure 29: Post processing setup

### 3.6.2 Pressure gradient

The first parameter investigated was the hydraulic behavior of the different test sections, comparing smooth and rough channel configurations.

To this end, the geometries were simulated both under standard (smooth wall) conditions and by applying a roughness model based on equivalent hydraulic parameters, with the aim of evaluating and optimizing the resulting pressure drop.

In order to ensure a consistent comparison between smooth and rough wall conditions, the analysis was restricted to the portion of the channel where the flow is fully developed. This approach allows for a clearer assessment of the pressure drop variation as a function of wall roughness.

As expected, the inclusion of geometric features and turbulence promoters leads to a significant increase in pressure drop. In particular, configuration 5.1 exhibits the highest pressure drop, followed by configuration 1.0, while configuration 1.1, representing a plain channel without turbulence promoters, shows the lowest values.

For a more general and scalable analysis, the pressure gradient (expressed in bar/mm) was also evaluated for both smooth and rough channels. This enables extrapolation of the pressure drop for channels of different lengths.

From the results reported in the following table, it can be observed that wall roughness systematically increases the pressure drop. However, for configuration 5.1 (characterized by a triangular fluid cross-section), the difference between smooth and rough wall conditions is less pronounced. This is likely due to the fact that the roughness parameters were calibrated based on configuration 1.1.

| | **Pressure drop $\Delta p$ (bar) - high $y^+$ ($\varepsilon = 60\mu m$)** | | | |
|---|---|---|---|---|
| **Sample** | **Smooth wall** | **Rough wall** | **$\Delta p/L$ smooth** ($bar/mm$) | **$\Delta p/L$ rough** ($bar/mm$) |
| Var1.1 | 2.68e-2 | 6.04e-2 | 4.47e-4 | 1.01e-3 |
| Var1.0 | 3.34e-1 | 6.93e-1 | 5.57e-3 | 1.16e-2 |
| Var5.1 | 2.18 | 2.22 | 3.63e-2 | 3.70e-2 |

Table 10: Pressure gradient smooth wall and rough wall

### 3.6.3 Fluid temperature profile

The second parameter analysed concerns the fluid temperature profile. In order to evaluate it, the thermal parameters associated with the roughness model implemented in STAR-CCM+ were adopted in the simulations. Since this model requires values of $y^+ > 30$, the temperature profile of the channel with the rough wall was considered in the fully developed flow region, starting from $x = 40$ mm.

From the figure, it can be observed that in the initial section of the pipe, up to approximately 40 mm, the different configurations exhibit a very similar trend; downstream of this section, however, more evident differences begin to appear among the cases. This justifies the choice of analysing the subsequent portion as a fully developed region. The comparison between the smooth and rough channels shows relatively limited differences: in the case of the rough wall, the fluid temperature increases by a few degrees, whereas for variant 1.1, namely the pipe without turbulence promoters, the roughness does not produce a particularly significant effect on the fluid thermal field.

For variants 1.0 and 5.1, the difference is even smaller. This can be attributed to the fact that the model parameters were calibrated on variant 1.1 and on its corresponding hydraulic diameter; therefore, in order to obtain more accurate results, a specific calibration for each hydraulic diameter would be necessary. As expected, variants 1.0 and 1.1, having the same specimen dimensions and identical inlet temperature conditions, exhibit the same outlet temperature, in agreement with the principle of energy conservation. On the other hand, variant 5.1, which is characterized by larger dimensions, shows a higher outlet temperature than the other two configurations.

The figure also clearly shows that the presence of turbulence promoters not only reduces the temperature of the solid, but at the same time also lowers the fluid temperature compared to the smooth case. This effect is due to the formation of vortices and recirculation zones, which promote mixing and fluid regeneration, thereby intensifying heat transfer. However, this thermal benefit is accompanied by an increase in pressure drop.

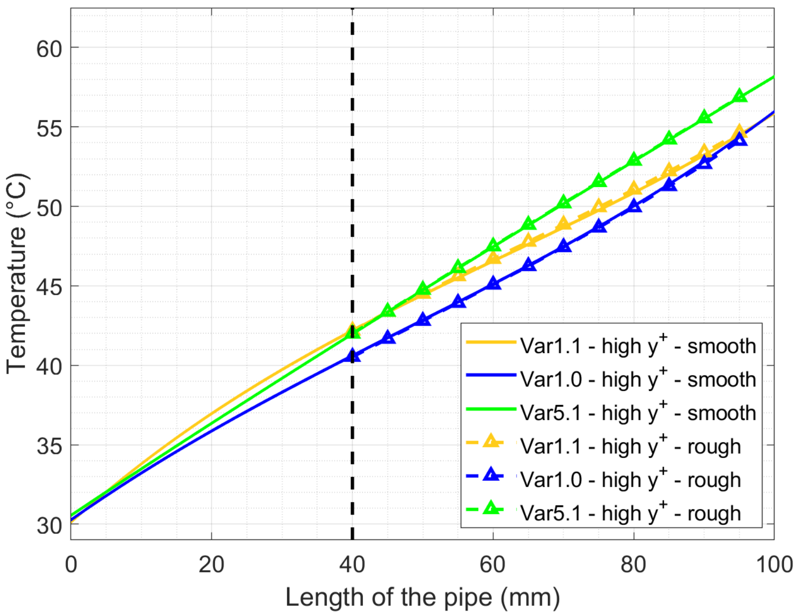


Figure 30: Fluid temperature profile with roughness

### 3.6.4 Solid temperature profile

The thermal parameters associated with the roughness model were used for the solid temperature analysis. As can be observed, the presence of roughness contributes to reducing the solid temperature along the entire specimen. This effect is due to the fact that, in addition to the turbulence promoters, the roughness itself induces stronger turbulence near the wall, promoting the formation of vortices and therefore enhancing the heat transfer between the fluid and the solid.

Compared with the smooth channel, the rough channel shows a reduction in solid temperature that remains significant and almost constant along the whole length of the specimen. In particular, the presence of the turbulence promoters leads to a marked decrease in solid temperature: when comparing variant 1.1, namely the channel without turbulence promoters, with the other two configurations, a reduction of the order of tens of degrees Celsius is observed, amounting to approximately 8-10%. Moreover, between variants 1.0 and 5.1, the solid temperature is lower in the case of variant 5.1, in agreement with the greater geometric complexity of the turbulence promoter; however, this configuration also leads to the highest pressure losses.

The curvature of the curves also suggests differences in the longitudinal heat-flux distribution: variant 1.1 shows a more pronounced increase in wall temperature up to a plateau, whereas the rough configurations tend to stabilise or slightly decrease after the fully developed region, indicating a greater local heat removal due to mixing and recirculation induced by the roughness. For variant 5.1, the difference between the smooth and rough channels is minimal for the solid, probably due to the combined effect of the different hydraulic diameter and the calibration of the roughness parameters, as discussed for the fluid temperature profile.

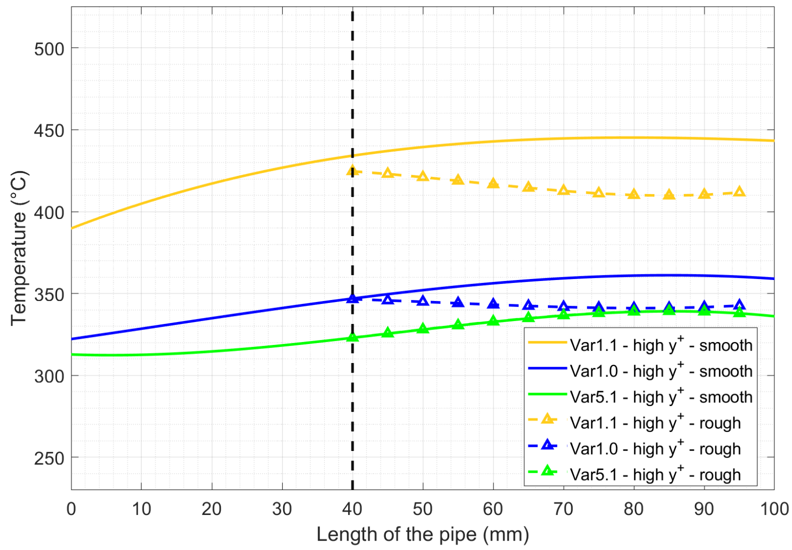


Figure 31: Wall temperature profile with roughness

### 3.6.5 Thermal-hydraulic properties smooth wall vs rough wall

As anticipated in the introduction to this chapter, the obtained results were compared with the simulations performed by the JSI research centre in Ljubljana, thus allowing a comparison between different CFD codes, since those simulations were carried out using ANSYS Fluent. In particular, in ANSYS Fluent the roughness was modelled using a low-$y^+$ approach with the addition of wall functions, which allows the effect of surface roughness on the wall to be represented. By contrast, in STAR-CCM+, as already discussed earlier, a wall-layer modelling approach with $y^+ > 30$ is required in order to apply the roughness model correctly.

The following table reports the comparison between the results obtained with the two simulation environments.

From the table, it can be observed that the pressure comparison is overall satisfactory between the two software packages, whereas the average temper-

| Smooth wall | | | | | | |
|---|---|---|---|---|---|---|
| | **Var1.1** | | **Var1.0** | | **Var5.1** | |
| **Parameter** | **PoliTo** | **JSI** | **PoliTo** | **JSI** | **PoliTo** | **JSI** |
| $\Delta p$ (bar) | 0.05 | 0.06 | 1.01 | 0.87 | 4.65 | 7.8 |
| $T_{fluid,ave}$ ($°C$) | 42 | 45 | 41 | 43 | 42 | 45 |
| $T_{solid,max}$ ($°C$) | 331 | 313 | 248 | 225 | 226 | 189 |

Table 11: CFD results comparison between PoliTo and JSI with smooth wall

| Rough wall ($\varepsilon = 60\mu m$) | | | | | | |
|---|---|---|---|---|---|---|
| | **Var1.1** | | **Var1.0** | | **Var5.1** | |
| **Parameter** | **PoliTo** | **JSI** | **PoliTo** | **JSI** | **PoliTo** | **JSI** |
| $\Delta p$ (bar) | 0.09 | 0.13 | 1.43 | 1.56 | 4.75 | 8.53 |
| $T_{fluid,ave}$ ($°C$) | 42 | 44 | 41 | 43 | 42 | 44 |
| $T_{solid,max}$ ($°C$) | 318 | 245 | 239 | 196 | 226 | 176 |

Table 12: CFD results comparison between PoliTo and JSI with rough wall

ature values are substantially in good agreement. On the other hand, more noticeable differences emerge for the maximum temperature. This suggests that comparing maximum quantities is not particularly meaningful, since such values are strongly influenced by the level of mesh refinement. It is therefore more appropriate to compare dimensionless and averaged quantities, such as the Nusselt number and the friction factor.

The next table reports the comparison of the Nusselt number and the friction factor, for both the smooth and the rough channels, for each specimen considered in the study.

This comparison clearly shows that roughness affects both the thermal and hydraulic behaviour, considering that a roughness height of 60 $\mu$m was sim-

| | Var1.1 | | Var1.0 | | Var5.1 | |
|---|---|---|---|---|---|---|
| **Parameter** | **Smooth** | **Rough** | **Smooth** | **Rough** | **Smooth** | **Rough** |
| $Nu$ | 191 | 234 | 174 | 212 | 221 | 222 |
| $f$ | 1.56e-2 | 3.51e-2 | 1.18e-1 | 2.41e-1 | 2.81e-1 | 2.86e-1 |

Table 13: Nusselt number and friction factor comparison between smooth and rough wall

ulated in the present study. The reduced difference between the smooth and rough channels is observed because the roughness parameters were calibrated based on the correlations and compared with variant 1.1. This highlights an important aspect, namely that the roughness parameters are strongly influenced by the hydraulic diameter and by the geometry of the turbulence promoter.

The table also confirms, as already discussed above, that turbulence promoters play a fundamental role in enhancing heat transfer, but at the same time they lead to an increase in hydraulic losses. It is therefore essential to find a compromise between improved thermal performance and the additional pumping power required.

## 3.7 Verification

In the absence of a direct experimental validation, it is necessary to verify that the numerical code used for the simulations is consistent with what is expected from the literature and from the available reference correlations. To this end, three separate verification steps were carried out, concerning the energy balance, the hydraulic behaviour, and the thermal behaviour of the model.

The first verification addressed the energy balance. In particular, it was checked that the energy supplied to the system, calculated as the heat flux applied to the heated surface, was equal to the energy removed by the fluid, evaluated through the enthalpy balance between mass flow rate and enthalpy rise between inlet and outlet:

$$\dot{Q}_{in} = \dot{m}\,(h_{out} - h_{in}) \tag{40}$$

where $\dot{Q}_{in}$ is the heat power supplied to the system and $\dot{m}(h_{out} - h_{in})$ represents the enthalpy increase of the fluid. As reported in the following table, the energy balance is satisfied, confirming the conservation of energy.

| **Energy conservation verification** | | | |
|---|---|---|---|
| **Parameter** | **Var1.1** | **Var1.0** | **Var5.1** |
| Power in (KW) | 6 | 6 | 7 |
| Power out (KW) | 6 | 6 | 7 |

Table 14: Energy conservation verification

The next step consisted in verifying the hydraulic parameter by comparing the friction factor for variant 1.1, namely the channel without turbulence promoters. The value obtained from the simulation was compared with the one provided by the Darcy-Weisbach relation:

$$f = \frac{2D_h \Delta p}{\rho L u_b^2} \tag{41}$$

where $f$ is the friction factor, $D_h$ is the hydraulic diameter, $\Delta p$ is the pressure drop, $\rho$ is the fluid density, $L$ is the channel length, and $u_b$ is the bulk velocity.

The simulated value was then compared with the explicit Haaland correlation:

$$\frac{1}{\sqrt{f}} = -1.8 \log_{10}\left[\left(\frac{\varepsilon/D_h}{3.7}\right)^{1.11} + \frac{6.9}{Re}\right] \tag{42}$$

where $\varepsilon$ is the equivalent roughness height and $Re$ is the Reynolds number. This correlation was used to include the effect of an equivalent roughness of 60 $\mu$m. The friction factor was evaluated in the fully developed region, from $x = 40$ mm to the end of the specimen. As shown in the following table, the two values are in good agreement, allowing the hydraulic behaviour of the model to be considered verified.

| **Friction factor verification (Var1.1)** | |
|---|---|
| **CFD simulation** | **Correlation** |
| 2.45e-2 | 2.46e-2 |

Table 15: Friction factor verification

Regarding the thermal parameter, the Nusselt number was verified by comparing the reference value obtained from the Gnielinski correlation, adopted as the benchmark, with the value extracted from the simulation:

$$Nu = \frac{(f/8)(Re - 1000)Pr}{1 + 12.7\sqrt{f/8}\,(Pr^{2/3} - 1)} \tag{43}$$

where $Nu$ is the Nusselt number, $f$ is the friction factor, $Re$ is the Reynolds number, and $Pr$ is the Prandtl number.

The Nusselt number from simulations was then obtained as:

$$Nu = \frac{D_h\, HTC}{k} \tag{44}$$

where $HTC$ is the convective heat transfer coefficient and $k$ is the thermal conductivity of the fluid.

| **Nusselt number verification (Var1.1)** | |
|---|---|
| **CFD simulation** | **Correlation** |
| 164 | 154 |

Table 16: Nusselt number verification

Also in this case, the comparison with the reference value shows good agreement, allowing the thermal parameter to be considered verified.

Overall, the results confirm the consistency of the numerical model from the energy, hydraulic, and thermal points of view.

# 4 Conclusions

In conclusion, this thesis work has made it possible to assess the potential of additively manufactured structures for heat exchanger applications operating under high thermal loads and particularly severe conditions. In particular, TPMS structures have emerged as a promising solution for enhancing heat removal capacity while maintaining hydraulic performance compatible with application constraints.

The CFD analyses were carried out using STAR-CCM+, while the TPMS geometries were generated with nTop. The specimen was investigated through numerical simulations in order to evaluate its thermal performance, keeping the heat load constant and varying the turbulence level, so as to highlight the influence of the turbulence promoters on the Nusselt number and the friction factor. Subsequently, a High Heat Flux Test was performed by imposing a heat load of 10 $MW/m^2$ and respecting the hydraulic limits prescribed for the W7-X fusion reactor. The results showed that the investigated structure is able to withstand such a load while remaining well below the material temperature limit and limiting the pressure drop to 2.67 bar, thus staying far below the 10 bar constraint imposed by the reactor.

In a subsequent stage, the heat load was further increased up to 20 $MW/m^2$, verifying that the TPMS specimen was still capable of operating under acceptable conditions. This result confirms the potential of the studied configuration as a promising solution even for more demanding scenarios.

Thanks to collaboration with the Max Planck Institute, the TPMS specimen was manufactured by additive manufacturing using LPBF (*Laser Powder Bed Fusion*) technology. This made it possible to conduct an experimental campaign at the Politecnico di Milano, aimed at validating the actual hydraulic behaviour of the specimen. The comparison between simulations and experiments showed that the simulated value, considering its associated uncertainty, falls within the experimental range. Since the simulations were performed assuming a smooth channel and did not account for the nominal roughness declared by the manufacturer, equal to 30 $\mu$m, it can be concluded that the print quality of the specimen is high. Consequently, the smooth case can be adopted as the baseline for subsequent simulations.

Nevertheless, it remains possible to consider structures characterised by higher roughness levels, for which the difference between the real configuration and the numerical model would no longer be negligible. Such a discrepancy could also be amplified by possible manufacturing defects. It is therefore necessary to further investigate the influence of roughness on the thermal and hydraulic properties of the specimen in future work.

Since roughness simulations in STAR-CCM+ require a high-$y^+$ boundary-layer modelling approach, the application of this methodology to TPMS geometries is particularly challenging due to the high tortuosity of the channels and the intense turbulence level. For this reason, specimens provided by the Max Planck Institute of Greifswald were used to evaluate the performance of the roughness model and to calibrate the related parameters, as well as to assess the extent to which roughness affects the thermal and hydraulic performance of the system.

Finally, the obtained results were also compared with independent simulations carried out by the JSI research institute in Ljubljana on the same specimens. This comparison showed that the roughness parameters are significantly influenced by the hydraulic diameter and by the geometry of the turbulence promoters. As a result, for a more accurate description of the phenomenon, future work will need to extend the analysis to new experimental campaigns and to a more specific calibration of the roughness models.

# Appendix A

# Least squares Grid Independence Index

The Grid Convergence Index (GCI) is a fundamental tool in *solution verification*, as it allows the numerical uncertainty associated with grid discretisation to be estimated. The method is based on Richardson extrapolation. In order for these tools to be applied reliably, two main conditions must be satisfied: first, the iterative error must be reduced to a level that is negligible with respect to the discretisation error; second, simulations must be performed on at least three computational grids, keeping a systematic refinement ratio $r$ defined as

$$r = \frac{h_{coarse}}{h_{fine}} \tag{45}$$

preferably greater than 1.3, in order to avoid possible numerical instabilities.

The procedure for estimating the uncertainty due to the mesh consists of five steps. First, the characteristic cell size $h$ is defined as the volumetric mean of the grid according to

$$h = \left( \frac{1}{n} \sum_{i=1}^{n} \Delta V_i \right)^{1/3} \tag{46}$$

where $n$ is the total number of cells and $\Delta V_i$ is the volume of the $i$-th cell. Next, the values of the quantity of interest are extracted on the three grids, denoted respectively as $\phi_1$, $\phi_2$, and $\phi_3$. From these values, the apparent order of convergence $p$ is determined, which allows Richardson extrapolation to be applied and the asymptotic exact solution for an infinitesimally fine grid to be estimated.

Once this value is known, the approximate relative error can be computed and, finally, the Grid Convergence Index can be evaluated with respect to the finest grid, according to

$$GCI_{fine}^{21} = \frac{F_s\, e_a^{21}}{r_{21}^{p} - 1} \tag{47}$$

where $e_a^{21}$ is the approximate relative error between grids 2 and 1, and $F_s$ is an empirical safety factor. According to the standard practice, the recommended value is $F_s = 1.25$ for analyses performed on at least three structured grids, whereas a more conservative value $F_s = 3$ is suggested for unstructured grids or in the presence of larger scatter in the results.

**GCI of manufactured gyroid sample**

| **GCI of gyroid sample** | | |
|---|---|---|
| **Parameter** | $\phi$ =**pressure (bar)** | $\phi$ =**temperature** ($^{\circ}C$) |
| $r_{21}$ | 1.27 | 1.27 |
| $r_{32}$ | 1.30 | 1.30 |
| $\phi_1$ | 9.20e-2 | 1.50e2 |
| $\phi_2$ | 9.17e-2 | 1.53e2 |
| $\phi_3$ | 9.13e-2 | 1.47e2 |
| GCI (%) | 1.87 | 2.69 |

Table 17: GCI of gyroid sample

### GCI of roughness sample

| GCI of roughness sample | | | |
|---|---|---|---|
| **Parameter** | $\phi$ =**pressure (bar)** | $\phi = \Delta T_{fluid}$ ($^{\circ}C$) | $\phi = \Delta T_{solid}$ ($^{\circ}C$) |
| $r_{21}$ | 1.61 | 1.61 | 1.61 |
| $r_{32}$ | 1.32 | 1.32 | 1.32 |
| $\phi_1$ | 2.66e-2 | 1.43e1 | 1.25e-1 |
| $\phi_2$ | 2.68e-2 | 1.42e1 | 1.20e-1 |
| $\phi_3$ | 2.70e-2 | 1.42e1 | 1.20e-1 |
| GCI (%) | 0.75 | 0.18 | 5.30 |

Table 18: GCI of roughness sample

# References

[1] M. Endler et al. "Wendelstein 7-X on the path to long-pulse high-performance operation". In: *Fusion Engineering and Design* 167 (2021), p. 112381. ISSN: 0920-3796. DOI: https://doi.org/10.1016/j.fusengdes.2021.112381. URL: https://www.sciencedirect.com/science/article/pii/S0920379621001575.

[2] O. Grulke et al. "Overview of the first Wendelstein 7-X long pulse campaign with fully water-cooled plasma facing components". In: *Nuclear Fusion* 64 (2024). OP2.1 long-pulse campaign; water-cooled divertor; detachment; 1.3 GJ 480 s example, p. 112002. DOI: 10.1088/1741-4326/ad2f4d.

[3] Max Planck Institute for Plasma Physics. *Wendelstein 7-X*. 2026. URL: https://www.ipp.mpg.de/w7x.

[4] T. Sunn Pedersen et al. *First results from divertor operation in Wendelstein 7-X*. Tech. rep. OP1.2a test-divertor results; pellet fueling; detachment; heat-flux patterns; preprint. EUROfusion preprint / internal report, 2018.

[5] J. Fellinger et al. "Tungsten based divertor development for Wendelstein 7-X". In: *Nuclear Materials and Energy* 37 (2023). Design and manufacturing routes for W-based divertor; CuCrZr heat sink, LPBF, HIP, coatings, thermal-mechanical analyses, p. 101506. DOI: 10.1016/j.nme.2023.101506.

[6] Alessio Quamori Tanzi et al. "Design of a 10 MW/m2-heat-flux removal system for a W7-X divertor tile using triply periodic minimal surfaces". In: *Case Studies in Thermal Engineering* 63 (2024), p. 105405.

[7] Laura Savoldi et al. "Use of Triply Periodic Minimal Surface Lattices for Heat Transfer Applications: A Systematic Literature Investigation". In: *Energies* 19.3 (2026). ISSN: 1996-1073. DOI: 10.3390/en19030833. URL: https://www.mdpi.com/1996-1073/19/3/833.

[8] Francesco Carrone et al. "Multi-scale lumped modeling of micro-channels cooling structure for W7-X divertor unit target module". In: *Fusion Engineering and Design* 204 (2024), p. 114481. ISSN: 0920-3796. DOI: https://doi.org/10.1016/j.fusengdes.2024.114481. URL: https://www.sciencedirect.com/science/article/pii/S092037962400334X.

[9] Mohamad Ziad Saghir et al. "Study of the thermal and hydraulic performance of porous block versus gyroid structure: Experimental and numerical approaches". In: *Energies* 17.4 (2024), p. 861.

[10] Wei Tang et al. "Analysis on the convective heat transfer process and performance evaluation of Triply Periodic Minimal Surface (TPMS) based on Diamond, Gyroid and Iwp". In: *International Journal of Heat and Mass Transfer* 201 (2023), p. 123642.

[11] Martin Beer and Radim Rybár. "Numerical study of fluid flow in a gyroid-shaped heat transfer element". In: *Energies* 17.10 (2024), p. 2244.

[12] Hyejun You et al. "Enhancement of heat transfer in cooling channels for electronic devices using multi-directional graded triply periodic minimal surfaces (TPMS)". In: *International Communications in Heat and Mass Transfer* 159 (2024), p. 108278.

[13] Mohamad Modrek et al. "Multi-objective topology optimization and numerical investigation of heat sinks based on triply periodic minimal surface lattices". In: *Case Studies in Thermal Engineering* 63 (2024), p. 105255.

[14] nTopology Inc. *nTop*. Software. 2025. URL: www.ntop.com.

[15] Guanghan Yan et al. “Experimental study on flow and heat transfer performance of triply periodic minimal surface structures and their hybrid form as disturbance structure”. In: *International Communications in Heat and Mass Transfer* 147 (2023), p. 106942.

[16] Hong Xu et al. “Flow and heat transfer performance of bionic heat transfer structures with hybrid triply periodic minimal surfaces”. In: *Applied Energy* 351 (2023), p. 121847.

[17] Danish Ansari and Christophe Duwig. “A gyroid TPMS heat sink for electronic cooling”. In: *Energy Conversion and Management* 319 (2024), p. 118918.

[18] Zhilong Cheng et al. “Investigations on porous media customized by triply periodic minimal surface: Heat transfer correlations and strength performance”. In: *International Communications in Heat and Mass Transfer* 129 (2021), p. 105713.

[19] Collins Chike Kwasi-Effah, Osezua Ibhadode, and Ahmed Qureshi. “Thermo-hydraulic performance characteristics of novel G-Prime and FRD Triply Periodic Minimal Surface (TPMS) geometries”. In: *International Communications in Heat and Mass Transfer* 159 (2024), p. 108226.

[20] Abdallah Barakat and BeiBei Sun. “Enhanced convective heat transfer in new triply periodic minimal surface structures: Numerical and experimental investigation”. In: *International Journal of Heat and Mass Transfer* 227 (2024), p. 125538.

[21] Mohammad Asif and Carlos A Grande. “TPMS contactors designed with imprinted porosity: numerical evaluation of momentum and energy transport”. In: *Industrial & Engineering Chemistry Research* 61.50 (2022), pp. 18556–18566.

[22] Wei Tang et al. "A novel convective heat transfer enhancement method based on precise control of Gyroid-type TPMS lattice structure". In: *Applied Thermal Engineering* 230 (2023), p. 120797.

[23] Mohamad Ziad Saghir and Mohammad M Rahman. "Effectiveness in Cooling a Heat Sink in the Presence of a TPMS Porous Structure Comparing Two Different Flow Directions". In: *Fluids* 9.12 (2024), p. 297.

[24] Eleonora Gajetti et al. "A new efficient mirror cooling for the transmission line of fusion reactor ECH systems based on triply periodic minimal surfaces". In: *IEEE Transactions on Plasma Science* 52.9 (2024), pp. 3765–3771.

[25] Esa Dube Kerme et al. "Experimental investigation of porous gyroid structure: Effect of cell size and porosity on performance". In: *Thermal Science and Engineering Progress* 53 (2024), p. 102728.

[26] Sean Samson, Phuong Tran, and Pier Marzocca. "Design and modelling of porous gyroid heatsinks: Influences of cell size, porosity and material variation". In: *Applied Thermal Engineering* 235 (2023), p. 121296.

[27] Abdallah Barakat and BeiBei Sun. "Controlling TPMS lattice deformation for enhanced convective heat transfer: A comparative study of Diamond and Gyroid structures". In: *International Communications in Heat and Mass Transfer* 154 (2024), p. 107443.

[28] Martin Beer and Radim Rybár. "Optimisation of heat exchanger performance using modified Gyroid-based TPMS structures". In: *Processes* 12.12 (2024), p. 2943.

[29] Fraunhofer IGCV. *Additive Manufacturing (AM)*. Accessed: 2026-07-13. 2025. URL: https://www.igcv.fraunhofer.de/en/research/competences/additive_manufacturing_am.html.

[30] Siemens. *STAR-CCM+*. Software. 2023. URL: https://www.siemens.com/it-it/products/simcenter/fluids-thermal-simulation/star-ccm/.

[31] Marius Wirtz and Daniel Dorow-Gerspach. *High heat flux test in JUDITH*. Tech. rep. Forschungszentrum Juelich, 2024.

[32] National Instruments. *LabView, Version 2024 Q1, accessed 2025-08-12*. Software. 2024. URL: https://www.ni.com/labview.

[33] Botjan Konar et al. *Thermal-hydraulic analysis with CFD*. Tech. rep. DIV-W7X.S.3-T004-D001; thermal-hydraulic analysis; CFD; W7-X deliverable; version 1.0. Jožef Stefan Institute, 2024.

[34] Siemens Digital Industries Software Simcenter STAR-CCM+. *User Guide 2306*. 2023.

[35] Issam El Khadiri et al. "Comprehensive analysis of flow and heat transfer performance in triply periodic minimal surface (TPMS) heat exchangers based on Fischer-Koch S, PMY, FRD, and Gyroid structures". In: *International Communications in Heat and Mass Transfer* 156 (2024), p. 107617.

[36] Mohamad Khalil et al. "Forced convection heat transfer in heat sinks with topologies based on triply periodic minimal surfaces". In: *Case Studies in Thermal Engineering* 38 (2022), p. 102313.

[37] Tao Zhang et al. "Numerical study on the anisotropy in thermo-fluid behavior of triply periodic minimal surfaces (TPMS)". In: *International Journal of Heat and Mass Transfer* 215 (2023), p. 124541.

[38] R Difonzo et al. "Assessment of different RANS turbulence models in mini-channels for the cooling of MW-class gyrotron resonators". In: *International Journal of Heat and Mass Transfer* 193 (2022), p. 122922.

[39] Cecilia Piatti, Laura Savoldi, and Nima Fathi. "Numerical Assessment of Hydraulic Properties of Triply Periodic Minimal Surfaces Structures". In: *Verification and Validation*. Vol. 86748. American Society of Mechanical Engineers. 2023, V001T07A001.